The Thesis Committee for Richard Hillman Roberts III certifies that this is the approved version of the following thesis:

Optical and Vibrational Properties of Low-Symmetry Two-Dimensional Materials Under Compressive Strain

APPROVED BY

SUPERVISING COMMITTEE:

Deji Akinwande, Supervisor

Jung-Fu Lin

Optical and Vibrational Properties of Low-Symmetry Two-Dimensional Materials Under Compressive Strain

by

Richard Hillman Roberts III

THESIS

Presented to the Faculty of the Graduate School of

The University of Texas at Austin

in Partial Fulfillment

of the Requirements

for the Degree of

MASTER OF SCIENCE IN ENGINEERING

THE UNIVERSITY OF TEXAS AT AUSTIN

August 2019

Dedicated to Madeleine, Rich, Joanne, and Kate.

Acknowledgments

I wish to thank my supervisors Dr. Deji Akinwande and Dr. Jung-Fu Lin for this opportunity and the invaluable support and advice they have given me during my time at UT-Austin. I also wish to thank Dr. Desiderio Kovar, Dr. Donglei Fan, and Krista Seidel at the Texas Materials Institute for their guidance in the graduate program; Dr. Joon-Seok Kim and Xianghai Meng for their mentorship and friendship; and everyone in the Lin and Akinwande research groups for their generous help along the way.

Optical and Vibrational Properties of Low-Symmetry Two-Dimensional Materials Under Compressive Strain

Richard Hillman Roberts III, M.S.E.
The University of Texas at Austin, 2019

Supervisor: Deji Akinwande

Due to their remarkable mechanical and electronic properties, two-dimensional materials have been the subject of avid interest over the last decade and a half. The successful exfoliation of graphene in 2004 was a watershed moment, prompting search for new monolayered materials that could be used in the next-generation of electronic devices. While many of graphene's admirable traits—record-setting tensile strength, massless dirac fermions, among others—are a result of its highly symmetric "honeycomb" crystal structure, a new class of monolayered materials with low-symmetry structures has recently been gaining interest. Due to their uniquely anisotropic electronic and thermal properties, low-symmetry materials such as ReS_2 and phosphorene are promising candidate materials for thermoelectric and optoelectronic devices capable of leveraging their anisotropy. In this work, we examine the effect of pressure on monolayer ReS_2 and few-layer phosphorene to determine their suitability for strain-tuned and flexible electronic devices.

Table of Contents

List of Tables

List of Figures

Chapter 1

Introduction

1.1 Motivation

Tuning the electronic properties of semiconductors through strain has long been an important technique in device engineering[1–3]. Traditionally, strain-tuned devices have been achieved via epitaxially grown heterojunctions, wherein epitaxial strain induced by a small lattice mismatch between two material layers results in significant shifts in the electronic bandgap of the heterostructure[4]. Today, strain tuning continues to be an exciting area of research due to the growing interest in flexible electronic devices. From wearable medical equipment[5,6] to flexible solar cells[7–9] to the bendable displays currently on the market, there is a rapidly growing demand for materials that can both take advantage of and withstand applied strain. From a mechanical perspective, polymer-based electronics are appealing candidate materials for strain-tuned devices due to their superior elastic properties[10–12]. However, their electronic performance often trails well behind traditional inorganic device materials[13,14]. Monolayer semiconductors, on the other hand, offer a unique compromise between flexibility and electronic performance, making them promising materials for next-generation electronic devices.

Transition metal dichalcogenides (TMDs) are an exciting family of layered, van der Waals (vdW) semiconductors that are exfoliable to down to monolayer thickness. In monolayer form, they possess sizable direct bandgaps[15,16]

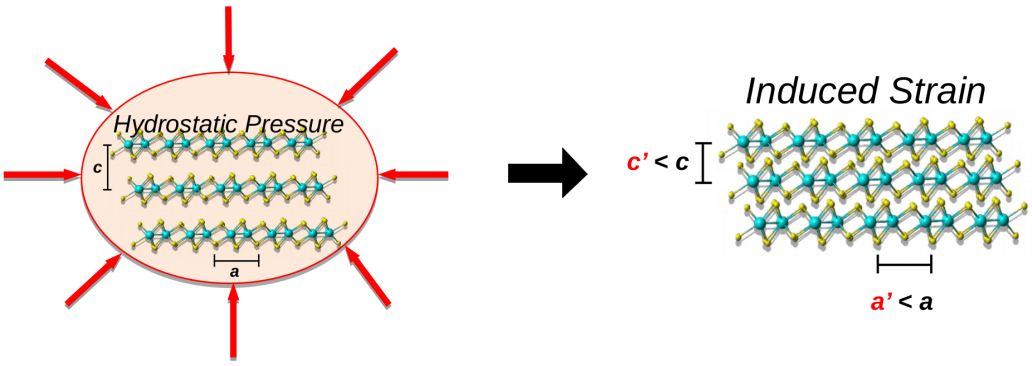

Figure 1.1: Illustration of the application of hydrostatic pressure to a layered van der Waals material; While the pressure is uniform, due the relative bonding strengths in the in-plane and out-of-plane directions the resulting strain is not necessarily isotropic—that is, $\Delta c \neq \Delta a$.

and electron mobilities in excess of 50 $cm^2/V{\cdot}s$ at room temperature[17,18]. TMDs also offer superb flexibility and measured strain limits above 20%[19]. Recent experimental and theoretical work has demonstrated how the electronic and vibrational properties of monolayer TMDs respond to various types of applied strain including uni- and bi-axial tensile strain[20–25], uni- and bi-axial compressive strain[21,22,26,25], and hydrostatic pressure[27–30]. Much of the work on monolayer TMDs to date has focused on MoS_2, WS_2, and their selenide counterparts which, similarly to graphene, possess high in-plane symmetry. Recently, however, lower-symmetry TMDs and elemental monolayers with anisotropic in-plane properties such as rhenium disulfide (ReS_2) and black phosphorus ("phosphorene" in monolayer form) have been garnering attention for their unique applications in polarization detectors[31–33], thermoelectrics[34,31,35], batteries[31,36,35], and photocatalysts[37–40].

Material anisotropy is a useful tool that is exploitable in electronic devices. Highly anisotropic materials such as ReS_2 and phosphorene have

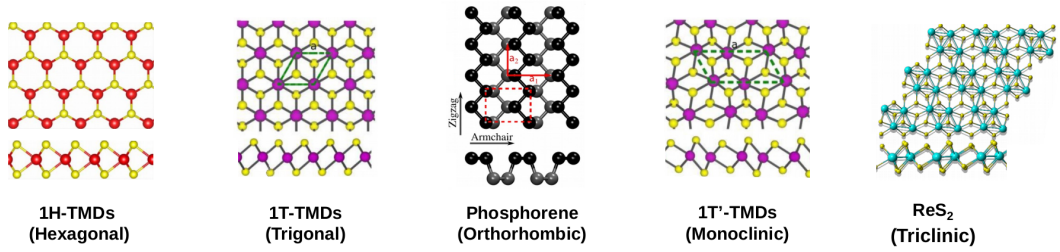

Figure 1.2: Crystal structures of common layered van der Waals semiconductors, ordered from highest to lowest symmetry; From left to right: 1H-TMDs[41], 1T-TMDs[28], phosphorene[42], 1T'-TMDs[28], and ReS_2, which adopts a distorted-3R phase.

different material properties along different crystallographic directions; thus, by changing the orientation of the material relative to an applied field, the response of the material is varied accordingly. A good example of this is the use of optically anistropic materials in photodetectors, which exhibit high responsiveness to the polarization of incident light[33]. In electronic applications, the anisotropic electronic and thermal transport properties of these materials can be utilized as well. For example, Liu et al.[43] show in their work how anisotropic transport in black phosphorus could be used to "route" heat and charge flow at the microscale to enhance thermoelectric performance.

1.2 Thesis Objectives

The objective of this research is to study the strain response of ReS_2 and black phosphorus/phosphorene, which belong to an emerging class of two-dimensional (2D) semiconductors with low symmetry and anisotropic material properties. We accomplish this by conducting optical experiments that are compatible with a high-pressure diamond anvil cell (DAC), applying strain values that range from those achievable in conventional devices (<10%) to

more extreme pressures up to tens of gigapascals. Our work provides insight into both the device engineering and high pressure physics of these unique materials.

Chapter 2

Experimental Methods

2.1 Synthesis and Preparation

Due to their weak interlayer interactions, van der Waals semiconductors can be exfoliated down to few- and monolayers of atoms. This was first demonstrated in graphene by Novoselov and Geim in 2004[44,45], which was famously achieved with Scotch tape and later awarded the Nobel Prize in Physics. Refinement of the exfoliation technique has enabled synthesis of a myriad of monolayer materials in graphene's wake.

In this work, we exfoliate ReS_2 and black phosphorus (BP) down to monolayer and few-layer forms, respectively. ReS_2 flakes with monolayer, bilayer, and multilayer regions are exfoliated using PVC film tape from Nitto, and transferred directly to a Si/Al_2O_3 substrate. Mild warming was used (~40°C) to facilitate transfer from the flake to the substrate. A similar method was used for BP, but due to the material's air stability, BP samples were immediately capped, either by:

1. Spin coating with PMMA (~200 nm)
2. Atomic layer deposition of Al_2O_3 (~25 nm)

Details of the two capping procedures can be found in previous work by our group[46].

For high-pressure experiments, samples were transferred from their initial substrates in one of several methods. For ReS_2, which did not require capping, samples could be transferred using a polydimethylsiloxane (PDMS) stamp transfer method developed by Kim et al.[47]. This method involves applying an adhesive layer to the stamp that can be melted at moderate temperatures. At room temperature, the stamp can be lowered down onto the sample aided by a confocal microscope. Once the sample adheres to the stamp, it is picked up and the stamp is then lowered onto the destination substrate (in our case the diamond culet, see Section 2.3). To ensure that the flake leaves the stamp, the stage of the setup is heated to melt the adhesive and release the sample on the new substrate. Any residual adhesive on the sample can then be removed with an organic solvent.

Since BP required capping for air-stability, transferring few-layer samples could not be achieved with the process described above. Here, after capping the sample with either PMMA or Al_2O_3, a small area around the sample (~100 μm) was carefully cleaved away from the substrate with a microscopically sharp tungsten carbide tip and subsequently transferred to the diamond culet with a needle. For thicker samples (>100 μm), the transfer process was done in a more straightforward "pick and place" fashion without cleaving the substrate, in which the sample was directly transferred using the tip of a needle under a microscope.

2.2 Characterization

Under ambient conditions, ReS_2 and BP were characterized via Raman and photoluminescence (PL) spectroscopy, atomic force microscopy (AFM), and transmission electron microscopy (TEM). Raman and PL spectroscopy are

particularly useful techniques to characterize 2D materials as they are fast and non-destructive. Moreover, 2D materials often exhibit layer-dependent optical and vibrational properties, making Raman and PL effective complements to AFM in determining the of thickness of the material.

Figure 2.1a shows the increase in optical bandgap of ReS_2 with decreasing layer number—a clear trend that is well replicated in literature[41,48,49]. Raman shifts also display a distinct trend with pressure, and even provide information on the stacking orientation of ReS_2: Qiao et al.[49] documented in their work how the difference in Raman shifts between two characteristic Raman modes $\Delta\omega$ depends on whether multilayer ReS_2 exhibits anisotropic-like (AI) or isotropic-like (IS) stacking, as shown in Figure 2.1b.

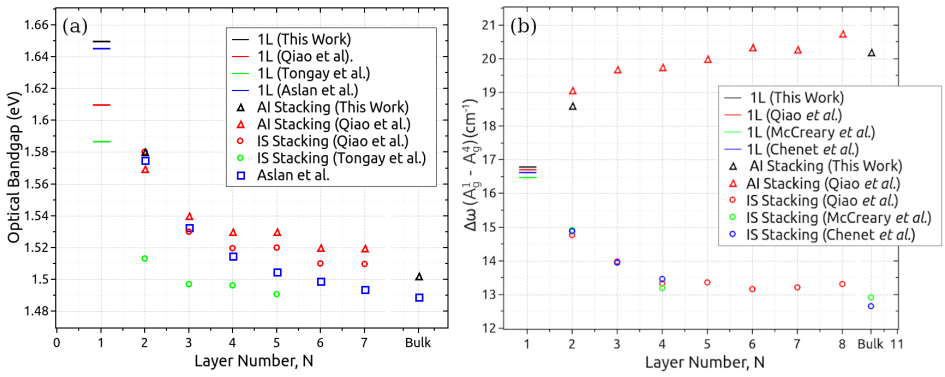

Figure 2.1: (a) Thickness dependence of the optical bandgap of ReS_2, compared with several datasets from literature[41,48,49]; (b) Thickness dependence of frequency difference $\Delta\omega$ between the A_g^1 and A_g^4 modes compared with literature values[41,48–51]; According to Qiao et al.[49], a reduction $\Delta\omega$ with decreasing layer number indicates that an ReS_2 sample with anisotropic-like stacking, while the opposite indicates isotropic-like stacking.

To enable reliable thickness determination of 2D materials via convenient optical methods, AFM must first be performed as a benchmark. An AFM

micrograph and height profile for an exfoliated ReS_2 flake with monolayer and bilayer regions are shown in Figure 2.2. Measurements were conducted using an Asylum MFP 3D system in tapping mode. The flake shown is roughly 15 μm in longest dimension with clean, sizable monolayer and bilayer regions. The height profile suggests an interlayer distance of ~0.8 nm for the bilayer region.

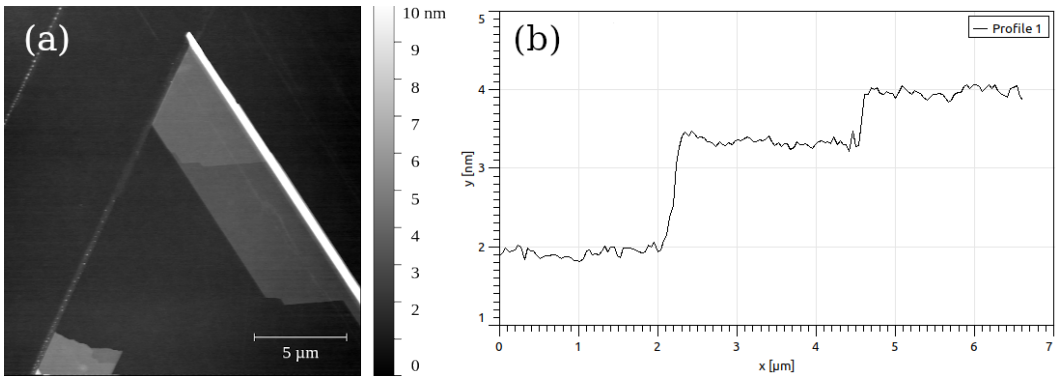

Figure 2.2: (a) Atomic force micrograph and (b) height profile of a ReS_2 flake with monolayer and bilayer regions; in (b), the substrate height is at ~2 μm, and the mono- and bilayer heights at ~3.3 and ~4.0 μm, respectively; the discrepancy between the interlayer spacing (~0.8 nm) and the substrate to monolayer height is due to the relative tip repulsion between the Si/Al_2O_3 substrate and the material itself—a result of using tapping mode AFM measurements[52,53].

With the thickness established via AFM, secondary thickness determinations such as Raman shifts and optical bandgaps can then be measured against AFM data to create reliable and fast thickness determinations for subsequent samples. Another secondary technique that is commonly used in this manner is simple optical microscopy: with AFM data and standardized substrates, microscope settings, etc., a reference database of thicknesses and material hues can be established[54].

2.3 High-Pressure Techniques

In a diamond anvil cell (DAC), pressures upwards of 500 GPa can be achieved, enabling an array of vital research under extreme conditions, including the quest to observe metallic hydrogen[55,56], study of the properties of the inner earth[57,58], and insight into the composition of remote planetary bodies[59–61]. To reach such pressures, DACs use diamonds with culet diameters as small tens of micrometers that compress a chamber filled with an inert pressure medium such as a noble gas. For all experiments described herein, neon gas is loaded into a short, symmetric DAC with 400-μm diameter culets via a custom gas loader designed and built in the mineral physics laboratory at UT-Austin.

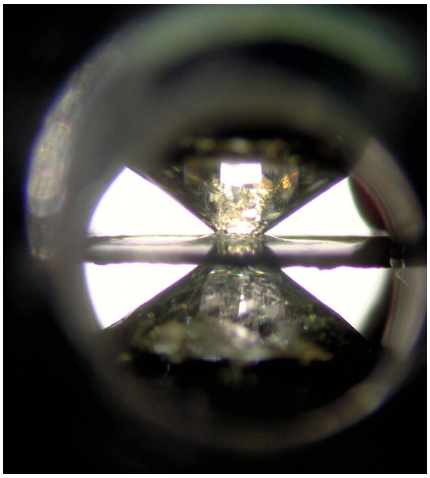

Figure 2.3: Photograph looking inside of a diamond anvil cell[62].

Visible in Figure 2.3 are the two opposing diamonds as well as the metal gasket that serves as the wall of the pressure chamber. The gasket is a flat piece of metal, typically a stainless steel or rhenium, with a drilled hole of diameter slightly less than the culet diameter. As the culets are pressed together, the

gasket collapses the volume of the chamber, applying pressure to the sample. A simplified schematic of a DAC is shown in Figure 3.1a.

While the primary benefit of using diamond anvils is their exceptional material hardness, they also provide a "window" for electromagnetic radiation. This allows us to view the sample as well as conduct optical measurements such and UV, Raman, IR, Brillouin, and PL spectroscopy. X-ray diffraction[63] and, in recent years, neutron diffraction[64] techniques are possible, as well. In this work, we employ primarily Raman, PL, and x-ray diffraction to study the vibrational, optoelectronic, and structural properties of ReS_2 and BP under pressure.

2.4 Polarized Light Spectroscopy

Polarized light spectroscopy (PLS) is an important technique for studying low-symmetry 2D materials. Previous work has used polarized Raman to determine the lattice orientation of ReS_2[50] and black phosphorus[65], probe anomalous vibrational properties in WTe_2[66], and to observed interactions between multi-walled carbon nanotubes under pressure[67]. Here we use the technique primarily to examine the evolution of vibrational anisotropy of monolayer and multilayer ReS_2 under compressive strain, but also to study few-layer phosphorene under in-plane tensile strain, bulk BP across an electronic phase transition, and the polarized excitonic emissions of multilayer ReS_2. Importantly, we present the first angle-resolved polarized Raman study under pressure in a diamond anvil cell. Figure 2.4 shows our custom rotation stage setup for PLS in measurements on a DAC, which has independently addressable x, y, z, and rotational axes.

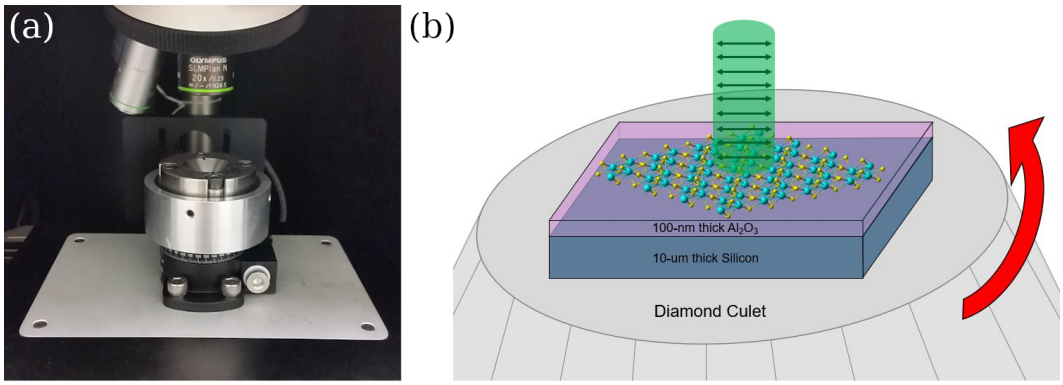

Figure 2.4: (a) Picture of the custom microscope stage used for polarized light spectroscopy measurements in this work, which has independent x, y, z, and rotation control; (b) Diagram of how a sample on a diamond culet is rotated with respect to incident laser polarization.

2.4.1 Raman

For polarized Raman experiments, a laser with a coherent incident polarization impinges on a sample with a known crystallographic orientation, and either parallel or perpendicular polarization are collected after scattering. For anisotropic materials, properties such as Raman scattering intensity and photoluminescence can be dependent on the angle between the polarization and crystal axis. The relative intensities can be modeled with the Raman tensor for a given vibrational mode. As an example, the A_g-type modes of BP have a Raman tensor given by:

$$R_{A_g} = \begin{bmatrix} a & 0 & 0 \\ 0 & b & 0 \\ 0 & 0 & c \end{bmatrix} \tag{2.1}$$

The Raman tensor elements a, b, and c are given by:

$$w = |w|e^{i\phi_w} \quad ; \quad \phi_w = \arctan \frac{\delta\epsilon''_{ww}/\delta q^{A_g}}{\delta\epsilon'_{ww}/\delta q^{A_g}} \quad ; \quad w = a, b, c \tag{2.2}$$

In general, the Raman intensity is proportional to $|\hat{e}_i \cdot R \cdot \hat{e}_s|^2$, where $\hat{e}_i$ and $\hat{e}_s$ are the incident and scattered polarization vectors, respectively. In the backscattering configuration with parallel incident and scattering polarization (denoted as $z(xx)\bar{z}$ in Porto's notation), which we use throughout:

$$\hat{e}_i = \hat{e}_s = \begin{bmatrix} \cos\theta & 0 & \sin\theta \end{bmatrix} \tag{2.3}$$

where θ is the angle between the incident polarization and a given crystallographic orientation. Finally, for the A_g-type modes of black phosphorus the intensity is given by:

$$I_{A_g} \propto \left(|a|\cos^2\theta + |c|\cos\phi_{ca}\sin^2\theta\right)^2 + |c|^2\sin^2\phi_{ca}\cos^4\theta \tag{2.4}$$

where $\phi_{ca} = \phi_c - \phi_a$. Radial plots of polarized Raman intensity take on "barbell-like" shapes in accordance with Equation 2.4, an example of which is shown in Figure 2.5, with θ measured every 10° from 0° to 360°.

2.4.2 Photoluminescence

Polarized PL is beginning to see more use in the analysis of anisotropic materials[48,68,69]. Similarly to polarized Raman, incident light with a well-defined orientation with respect to the crystallographic orientation of the material is used, and scattered light is filtered through a polarizer to collect either parallelly polarized or cross-polarized data. This technique is particularly useful for ReS_2, which has multiple excitonic transitions that selectively absorb

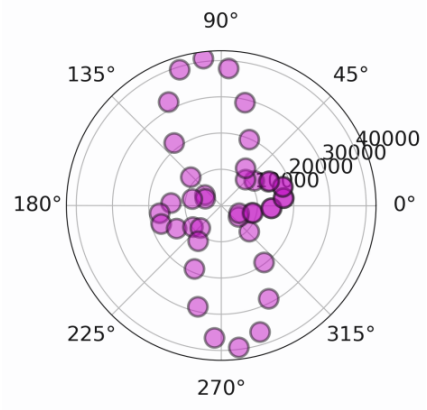

Figure 2.5: Example radial plot of polarized Raman intensity for the Raman-active A_g^1 mode of black phosphorus.

and emit linearly polarized light. Aslan et al.[48] first reported this behavior in 2016, which has subsequently made ReS_2 a promising material for wavelength-selective optoelectronic devices[68,69]. Since the two prominent excitons in multilayer ReS_2 exhibit nearly oppositely oriented polarization profiles, they can be thus be individually addressed using polarized light. Figure 2.6 shows both the full PL spectra at various incident polarization angles as well as the polarization profiles of the four excitonic transitions we observed.

2.4.3 Optical Interference in Birefringent Black Phosphorus

For thin films, optical interference must be considered when measuring polarization-dependent Raman or PL intensities. This is especially true for optically anisotropic (birefringent) materials, for which such effects may not contribute equally along different crystallographic directions. To address this concern, we present in this section an example analysis of the interference effect in black phosphorus thin films. What follows is an excerpted and lightly edited passage from the *Supplementary Information* of Zhu et al.[70], which was

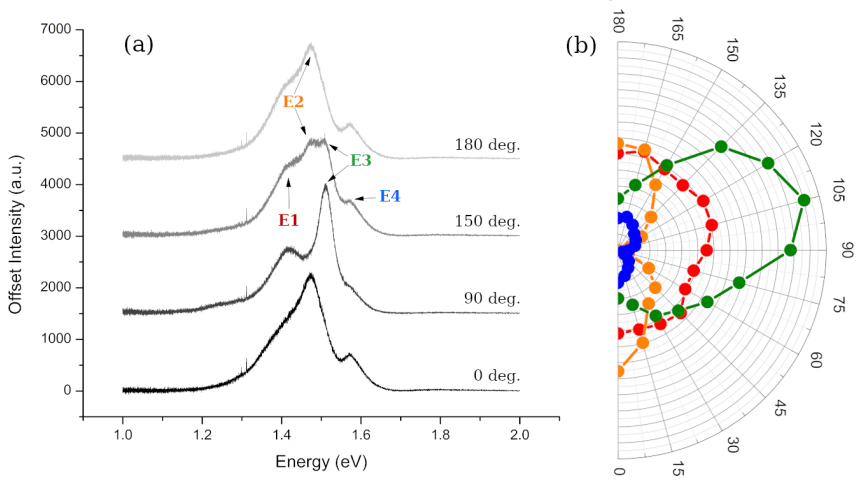

Figure 2.6: (a) Photoluminescence spectra of multilayer ReS_2 at various polarization angles with respect to the $\vec{b}$-axis of the material; Four peaks with excitonic line shapes are denoted as $E1$, $E2$, $E3$, and $E4$, with colors corresponding to the data shown in (b); (b) Radial plots of polarized photoluminescence intensity for each excitonic peak motioned in (a); Data points were gathered in 15° increments from 0 to 180°, with 0° corresponding to polarization parallel to the $\vec{b}$ axis of the material.

written by the author.

Due to the sample configuration—which consists of a thin black phosphorus (BP) layer (~10–15nm) transferred onto a nano-polyimide (NPI, ~60nm)/Pd (~50nm)/bulk polyimide (PI) substrate and capped with polymethyl methacrylate (PMMA) (~200nm) – optical interference effects will be present due to the varying refractive indices of the thin films. This effect is well documented in Ref. 71 for graphene on Si/SiO_2 substrates. Ref. 72 performs a similar analysis for BP on Si/SiO_2, while also considering the birefringence of the material (i.e., differing refractive indices along the zigzag (ZZ) and armchair (AC) directions). The measured Raman signal can be significantly impacted by this interference effect, which is dependent on the incident laser wavelength and the wavenumber of the measured Raman modes, in addition to the thin-layer thicknesses and refractive indices. In polarized Raman measurements of birefringent materials such as BP, the interference effect differs along different crystallographic orientations of the material, and must be considered to determine the intrinsic anisotropy of the material measured by polarized Raman.

In this work, we have generally followed the approach detailed in Ref. 72, in which the interference factor, F, is given by the absolute square of the scattering and absorption terms (F_{sc} and F_{ab}, respectively), integrated over the thickness of the BP sample, and multiplied by a normalization factor, as follows:

$$F = N \int_0^{d_1} |F_{ab}(x) F_{sc}(x)|^2 dx \tag{2.5}$$

$$F_{ab}(x) = t_{01} \frac{(1 + r_{12} r_{23} e^{-2i\beta_2^{ex}}) e^{-i\beta_x^{ex}} (r_{12} + r_{23} e^{-i\beta_2^{ex}}) e^{-i(2\beta_1^{ex} - \beta_x^{ex})}}{1 + r_{12} r_{23} e^{-2i\beta_2^{ex}} + (r_{12} + r_{23} e^{-2i\beta_2^{ex}}) r_{01} e^{-2i\beta_1^{ex}}} \tag{2.6}$$

$$F_{sc}(x) = t_{10}\frac{(1 + r_{12}r_{23}e^{-2i\beta_2^{sc}})e^{-i\beta_x^{sc}}(r_{12} + r_{23}e^{-i\beta_2^{sc}})e^{-i(2\beta_1^{sc}-\beta_x^{sc})}}{1 + r_{12}r_{23}e^{-2i\beta_2^{sc}} + (r_{12} + r_{23}e^{-2i\beta_2^{sc}})r_{10}e^{-2i\beta_1^{sc}}} \tag{2.7}$$

where N is the normalization factor given by the reciprocal of the interference factor for a free-standing BP sample (only air on both sides), and

$$t_{ij} = \frac{2n_i}{n_i + n_j}; \quad r_{ij} = \frac{n_i - n_j}{n_i + n_j} \tag{2.8}$$

are the Fresnel coefficients for the interface of the i^{th} and j^{th} layers, and

$$\beta_x^{ex} = \frac{2\pi x n_1}{\lambda_{ex}}; \quad \beta_x^{ex} = \frac{2\pi x d_i n_i}{\lambda_{ex}}; \quad \beta_x^{sc} = \frac{2\pi x n_1}{\lambda_{sc}}; \quad \beta_x^{sc} = \frac{2\pi x d_i n_i}{\lambda_{sc}} \tag{2.9}$$

where n_i is the complex refractive index for the i^{th} layer, d_i is the thickness of the i_{th} layer, x denotes the depth in the sample layer ($i = 1$), and λ_{ex} and λ_{sc} denote the wavelength of incident and Raman scattered light, respectively.

For BP, we consider two scattering factors: one calculated using the refractive index along the ZZ-direction and another using the refractive index along the AC-direction (F_{ZZ} and F_{AC}, respectively). The ratio of these two interference factors indicates the degree to which polarized Raman plots are artificially enhanced/diminished when light is polarized parallel one of these directions. A ratio of $\frac{F_{ZZ}}{F_{AC}} = 1$ indicates that the interference effect contributes equally in both crystallographic directions, and thus interference effects on the anisotropic Raman response of the material can be neglected.

Eqns. 2.6 and 2.7 take into account three interfaces: the interface between the environment and BP (i,j = 0,1), between BP and the layer below

it (i,j = 1,2), and one additional interface (i,j = 2,3). Our sample configuration has five interfaces: Air/PMMA, PMMA/BP, BP/NPI, NPI/Pd, and Pd/PI. Deriving equations analogous to Eqns. 2.6 and 2.7 for this number of interfaces is nontrivial, and some simplifying assumptions were made to reduce the problem to only three interfaces. Firstly, we assume that all the light that reaches the thin, metallic Pd layer is reflected, and thus we ignore the Pd/PI interface. Secondly, we consider two situations: one in which the PMMA on top of BP is ignored ("air environment") and another in which we treat the PMMA layer as infinitely thick ("PMMA environment"). We then calculate interference factors for both situations to determine the "worst-case" scenario, in which the ratio of the interference factors is largest. Additionally, since there is some uncertainty in the thickness of the BP sample, we consider both 10-nm and 15-nm BP layers for both aforementioned scenarios to find the overall worst-case interference.

For 10- and 15-nm BP in a PMMA environment, the difference in interference factors F_{ZZ} and F_{AC} was determined to be ~1.5% and ~0.3%, respectively. For 10- and 15-nm BP in an air environment, the difference in interference factors F_{ZZ} and F_{AC} was determined to be ~0.75% and ~4.0%, respectively. Note: these values differ between different Raman modes, but by less than 0.05% in each case. Since the "worst-case" scenario (15-nm BP sample in an air environment) has a difference of interference factors along different crystallographic directions of less than 5%, we determined interference effects in our sample configuration are mostly negligible. To illustrate this, we have fit our polarized Raman data to functions for the Raman intensity as a function of polarization angle based on the Raman tensor for Ag-symmetry modes in BP, again following the procedure outlined in Ref. 72. We then corrected these

fits to reflect the interference factors calculated for the worst-case interference scenario, for comparison. It is clear from Figure 2.7b-e that the interference effect is negligible compared to experimental error and, importantly, the change in anisotropy of the polarized Raman plots due to strain.

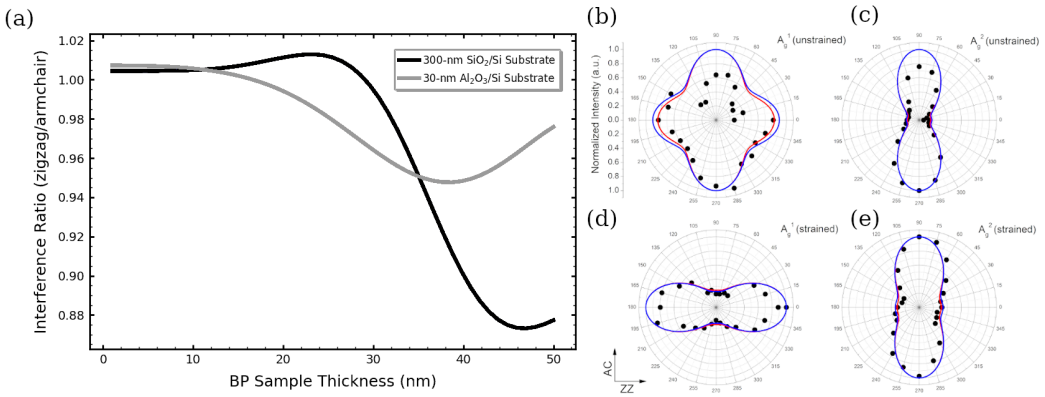

Figure 2.7: (a) Model of interference ratio ($F = ZZ/AC$) as a function of sample thickness for black phosphorus on 300-nm Si/SiO_2 (black line) and 30-nm Si/Al_2O_3 (gray line) substrates; (b-e) Experimental polarized Raman data (black circles) on few-layer black phosphorus in (b,c) with and (d,e) without in-plane tensile strain; Blue lines show fits to data based on Raman tensor; Red lines are corrected fits based on the interference ratio in (a).

The interference effects in our sample configuration are much less pronounced than those calculated in Ref. 72 due to the difference of refractive indices of the substrate in capping layers used. Considering the non-BP layers, one would expect that those with refractive indices deviating most from the refractive index of the environment would have the largest contribution to the interference effect. In the case of Ref. 72, Silicon has a real part of the refractive index that is >300% larger than that of the environment (air). Contrast this with our configuration, where the non-BP layer with the largest refractive index is PI, which has a refractive index that is 70% larger than that of the air

environment – or 14% larger than the PMMA environment (Table 2.1).

Refractive Index	Air Environment	PMMA Environment	Kim et al.[72]
Air	1		1
PMMA[73]		1.49	
BP (ZZ)[74]	$3.74-i0.52$	$3.74-i0.52$	$3.74-i0.52$
BP (AC)[74]	$3.74-i0.52$	$3.74-i0.52$	$3.74-i0.52$
PI[75]	1.7	1.7	
Pd[75]	1.588	1.588	
SiO_2[76]		1.47	
Si[77]			$4.46-i0.05$

Table 2.1: Refractive indices of materials considered in our analysis of the optical interference effect of black phosphorus, grouped by a given experimental environment (i.e. the combination of substrate, sample, and capping material, if applicable); Literature values for refractive indices are either directly from the references listed or extrapolated from the same.

While this analysis is specific to the material system and experimental environment considered here, it can be easily generalized to other systems to determine if and how interference effects from thin films will affect optical measurements. As can be seen in Figure 2.7a, the effect can often be ignored for extremely thin samples. For sufficiently thick samples ($t >> \lambda_{light}$) the effect is also negligible.

Chapter 3

Results and Discussion

3.1 High-Pressure Studies of Rhenium Disulfide

3.1.1 Background

ReS_2 is a particularly exciting anisotropic material due to its air stability[78] and myriad of compelling structural, optical, electronic, and vibrational properties. It has a low-symmetry crystal structure (triclinic, space group $P\bar{1}$) that is commonly referred to as the $1T'$ phase in literature, though recent work has proposed the nomenclature "distorted-$3R$" phase[79]. This unique structure is brought about by a Peierls distortion in which Re atoms form pseudo-1D chains along the $\vec{b}$-axis of the material, resulting in highly anisotropic in-plane electronic[80] and thermal[81] transport, as well as optical birefringence[48]. ReS_2 also exhibits a flat electronic band structure with several local conduction (valence) band minima (maxima)[82,83]. This has contributed to disagreement regarding the nature of the bandgap of ReS_2[41,48]—an issue further complicated by the various stacking orientations adopted by the multilayer form[49,84]. Recent studies suggest that ReS_2 is a marginally indirect bandgap semiconductor in the bulk[48,82,85,83,86], but there is still disagreement over nature of the bandgap in the bi- and monolayer limit[82,86].

Vibrationally, ReS_2 has 18 Raman-active modes, all with A_g-type symmetry and varying intensity depending on the polarization and wavelength of incident light. The polarized Raman response under ambient conditions has

been well documented in the literature[50,87,88,51]. Due to the lower symmetry of the material, the Raman modes of ReS_2 do not exhibit the same *strictly* in-plane or out-of-plane vibrational character as MoS_2, for example. However, several modes can be described as consisting of predominantly in-plane or out-of-plane vibrations[51]. For the lower-frequency, Re-dominant vibrations, A_g^4 (132 cm^{-1}) and A_g^5 (143 cm^{-1}) are considered predominantly out-of-plane modes, while the A_g^1 (153 cm^{-1}), A_g^6 (162 cm^{-1}), A_g^7 (213 cm^{-1}), A_g^8 (235 cm^{-1}) predominantly in-plane.

While several theoretical studies have examined the electronic and vibrational strain response of ReS_2[89–91], few experimental works have been published to date. Yang et al.[67] generated local strain in multilayer ReS_2 via an elastomeric substrate, modulating the bandgap and inducing magnetism in the material; Tongay et al.[41] examined the Raman response of multilayer ReS_2 to hydrostatic pressure (compressive strain) up to 7.0 GPa in a diamond anvil cell (DAC), finding the material's vibrational properties to be less sensitive to pressure than other TMDs; and Yan et al.[92] measured both the Raman and photoluminescence (PL) response of multilayer ReS_2 up to 33.7 and 9.0 GPa, respectively, in a DAC.

A single ReS_2 flake with mono-, bi-, and multilayer regions was mechanically exfoliated from a bulk crystal (2D Semiconductors) and transferred to a 10-μm/100-nm silicon/Al_2O_3 substrate placed onto the diamond culet of a DAC via the PDMS transfer method described in Kim et al.[47]. The thickness of flake region was determined via atomic force microscopy, Raman, and PL measurements (Figure S1). For pressure experiments, a DAC with 400-μm diameter culets was loaded with an inert Ne gas pressure medium, a ruby sphere for pressure calibration, and a Re gasket that served as the pressure chamber.

Figure 3.1a shows an illustration of the DAC and the sample configuration on the diamond culet. Optical images of the sample prior to transfer and after loading and pressurizing the cell are shown in Figure 3.1b.

Before transferring the sample to the DAC, PL and Raman spectra were measured under ambient conditions for each thickness (Figure 3.1c-d). Lorentzian fitting of the PL spectra for monolayer and bilayer regions reveal a single excitonic peak shape at 1.65 and 1.58 eV, respectively. The bulk region displays three excitonic peaks at 1.39, 1.50, and 1.56 eV, which are identified as the indirect bandgap, Exciton 1, and Exciton 2, respectively[48]. The exciton positions for each thickness are marked with vertical lines in Figure 3.1d. As Exciton 1 gives the largest PL intensity and persists after application of pressure, it is referred to as the optical bandgap E_g of the multilayer region throughout this work. Our pre-transfer E_g values for all thicknesses agree quite well with those reported in literature[41,48,49], though we note that PL measurements after transferring the sample to the DAC—but before pressurization—show a small decrease in E_g for each thickness. This can be attributed to strain relaxation from the transfer process[94].

Table 3.1 shows the measured E_g as well as Raman shifts ω for the six lowest frequency modes, for which we adopt the naming convention of Pradhan et al.[95]. Based on the thickness dependence of the Raman modes, and particularly $\Delta\omega$ of A_g^1 and A_g^4 modes, we conclude that the stacking type of the exfoliated flake is the anisotropic-like (AI) stacking reported by Qiao et al.[49] (Figure S2). The six lowest-frequency modes of ReS_2 are predominantly Re atom vibrations, and exhibit the largest Raman intensities of the 18 active modes under the experimental conditions (532-nm laser light with incident polarization parallel to the b-axis of the material) over the pressure range

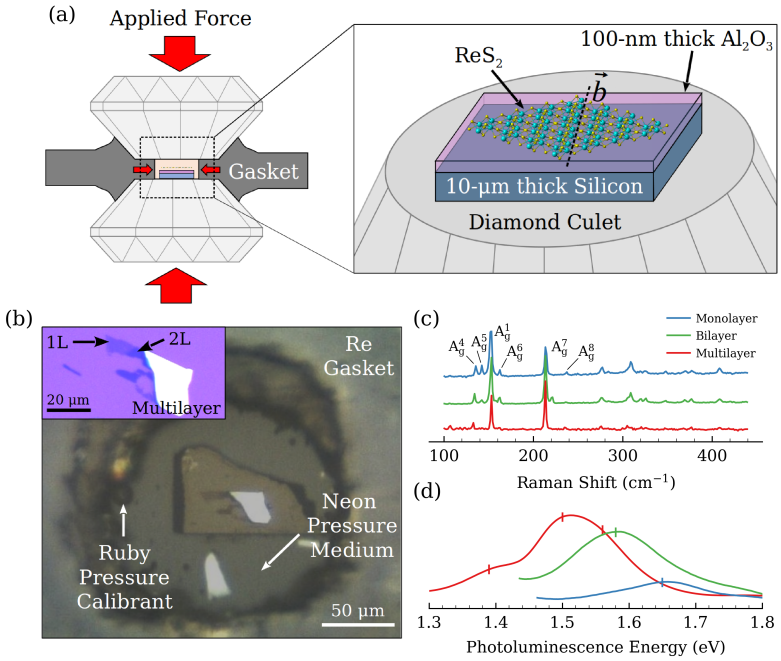

Figure 3.1: (a) Illustration of a diamond anvil cell (DAC) adapted from Ref. 93 and inset depicting a monolayer ReS_2 sample on an Si/Al_2O_3 substrate placed on the diamond culet. (b) Optical image of exfoliated ReS_2 flake with mono-, bi-, and multilayer regions on a Si/Al_2O_3 substrate loaded into a DAC with a ruby pressure calibrant and Ne gas as a pressure medium; a Rhenium gasket facilitates the application of pressure generated by squeezing together the diamond culets; (inset) Optical image of the same sample prior to transferring to the DAC. (c) Raman and (d) Photoluminescence (PL) spectra of the mono- (blue), bi- (green), and multilayer (red) ReS_2 samples examined in the study; in (c), six of the material's 18 Raman active modes are labeled; Vertical lines in (d) denote exciton peak positions determined from Lorentzian fitting of PL spectra.

considered.

Table 3.1: Ambient optical bandgaps and Raman shifts for mono-, bi-, and multilayer ReS_2 obtained from the Lorentzian fits to Raman and PL spectra; Optical bandgaps both before and after PDMS transfer to the DAC are shown; Raman shifts were measured post-transfer, but prior to pressurizing the DAC.

		Raman Shift, ω (cm^{-1})					
	Optical Gap E_g (eV)	A_g^4	A_g^5	A_g^1	A_g^6	A_g^7	A_g^8
1L	1.65	135.4	142.4	152.1	161.9	213.6	236.7
2L	1.58	133.7	145.0	152.6	161.8	213.3	236.0
Mult.	1.50	132.1	142.8	152.6	161.7	212.9	235.2

3.1.2 Opto-Electronic Properties

3.1.2.1 Optical Bandgap

After pressurizing the cell, Raman and PL measurements were conducted at various pressures up to 13.6 GPa. For multilayer ReS_2, a PL signal was discernible above the background up to 10.3 GPa, while monolayer and bilayer signals were only observed up to 4.0 GPa (Figure 3.2). The loss of PL signal with increasing pressure has been interpreted as a direct-to-indirect band transition in other TMD systems[28,29]. For ReS_2, however, the picture is more complicated.

As previously noted, three excitonic peaks were observed for the multilayer region before the application of pressure: the indirect gap (1.39 eV), Exciton 1 (1.50 eV), and Exciton 2 (1.56 eV). After application of pressure, the indirect gap was observed only up to 0.6 GPa (Figure S3); beyond this pressure, Exciton 1 is the lowest energy gap observed. Since Exciton 1 has a direct gap[48], our data suggest that under only modest compressive strain multilayer ReS_2 becomes a direct gap semiconductor. This is a significant finding, as a

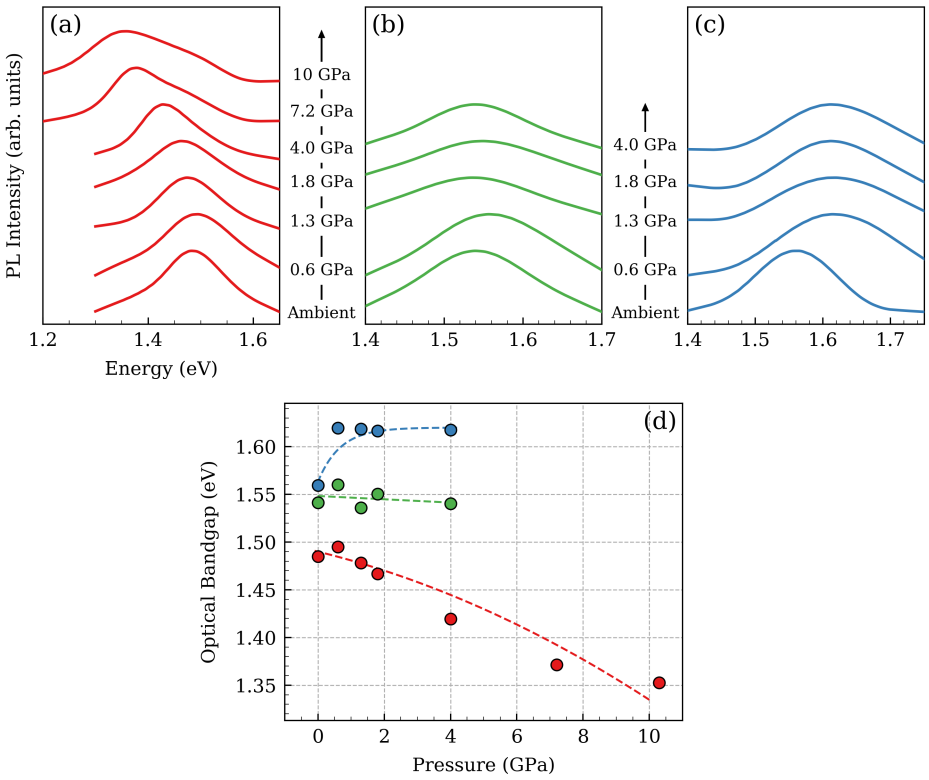

Figure 3.2: PL spectra of (a) multilayer, (b) bilayer, and (c) monolayer ReS_2 samples at various pressures; the PL signal of the multilayer sample was visible up to ~10 GPa, while bi- and monolayer signals were only distinguishable from the background up to ~4 GPa. (d) Optical bandgap vs. pressure for all ReS_2 samples, determined by fitting the spectra shown in (a–c), with monolayer, bilayer, and multilayer samples shown with blue, green, and red circles, respectively, with dashed lines to guide to the eye.

direct-gap multilayer ReS_2 would be more suitable for optoelectronic applications. We note that this result differs from Yan et al.[92], which reports that the indirect gap persists up to ~5 GPa. Regardless, it is clear that compressive strain tuning can selectively alter the nature of the bandgap in multilayer ReS_2, and potentially at strain values easily achievable in conventional device applications.

At 4 GPa, another peak emerges in the multilayer spectra at slightly higher energy than Exciton 1 (Figure 3.2a and S3), and persists until 10 GPa, after which no PL signal is discernible from the background. The Lorentzian line shape suggests that this peak is also excitonic nature, though the exact transition was not identified in this work. Both monolayer and bilayer spectra were well fit by single Lorentzian curves throughout the pressure range examined, though signals were generally weak and significantly broader compared with the multilayer spectra (Figure 3.2b-c). The weak signal intensities relative to multilayer suggest that monolayer and bilayer ReS_2 are likely indirect gap semiconductors throughout the pressure range considered. This is consistent with the low PL quantum yields recently reported by Mohamed et al.[86].

Figure 3.2d shows E_g for each thickness as a function of pressure. For monolayer ReS_2, E_g blueshifts slightly with pressure, from 1.56 eV under ambient conditions to 1.62 eV at 4.0 GPa. For multilayer, E_g redshifts from 1.48 eV to 1.35 eV at 10.3 GPa. Bilayer ReS_2 displays a nearly constant E_g of ~1.5 eV from ambient pressure to 4 GPa. Linear fits to experimental values of E_g vs. pressure yield tuning rates $\Delta E_g/\Delta P$ of 9.2, -1.7, and -14.7 meV/GPa, for mono-, bi-, and multilayer thicknesses, respectively. We note that the linear fits are meant to give an approximate tuning rate for engineering purposes, and not to make any determinations about the deformation potentials of the

band structure.

3.1.3 Vibrational Properties

Experimental Raman shifts display only a modest response to pressure (Figure 3.3d). For all six of the Raman modes examined in this study, Raman shifts harden roughly linearly from ambient pressure to 13.6 GPa. The average experimental hardening rates $\Delta\omega/\Delta P$ of in-plane modes for mono-, bi-, and multilayer ReS_2 are 1.20, 1.22, and 1.21 cm^{-1}/GPa, respectively, while out-of-plane $\Delta\omega/\Delta P$ are 0.53, 0.67, and 0.85 cm^{-1}/GPa, respectively.

We observe no obvious indication of a structural transition in the experimental Raman spectra, as Raman shifts for all thicknesses exhibit gradual, linear Raman mode hardening with no overt discontinuities or emergence of new modes up to 13.6 GPa. While this is ostensibly in conflict with the phase transition observed in bulk ReS_2 around 10–11 GPa[96,97], the absence of an obvious structural transition can be attributed to the thickness of the sample. It has been well documented that layered vdW materials are highly compressible in the out-of-plane direction—for example, the $\vec{c}$-axis in MoS_2[98–100]. Accordingly, structural evolutions often arise from the compression of these layers, which results in dramatic increases in interlayer bonding energy. Furthermore, past work has shown that such interlayer interactions *decrease* with layer number, as evidenced by increased interlayer distances and bandgaps upon thinning down to the monolayer limit[101–103]. It follows then that few-layer and monolayer vdW materials would require relatively higher strains to induce a phase transition, as more energy is required to strengthen the interlayer interactions. A clear example of this is the phase transition from the ambient A7 phase to the high-pressure A17 phase in phosphorene: while bulk black phosphorus undergoes

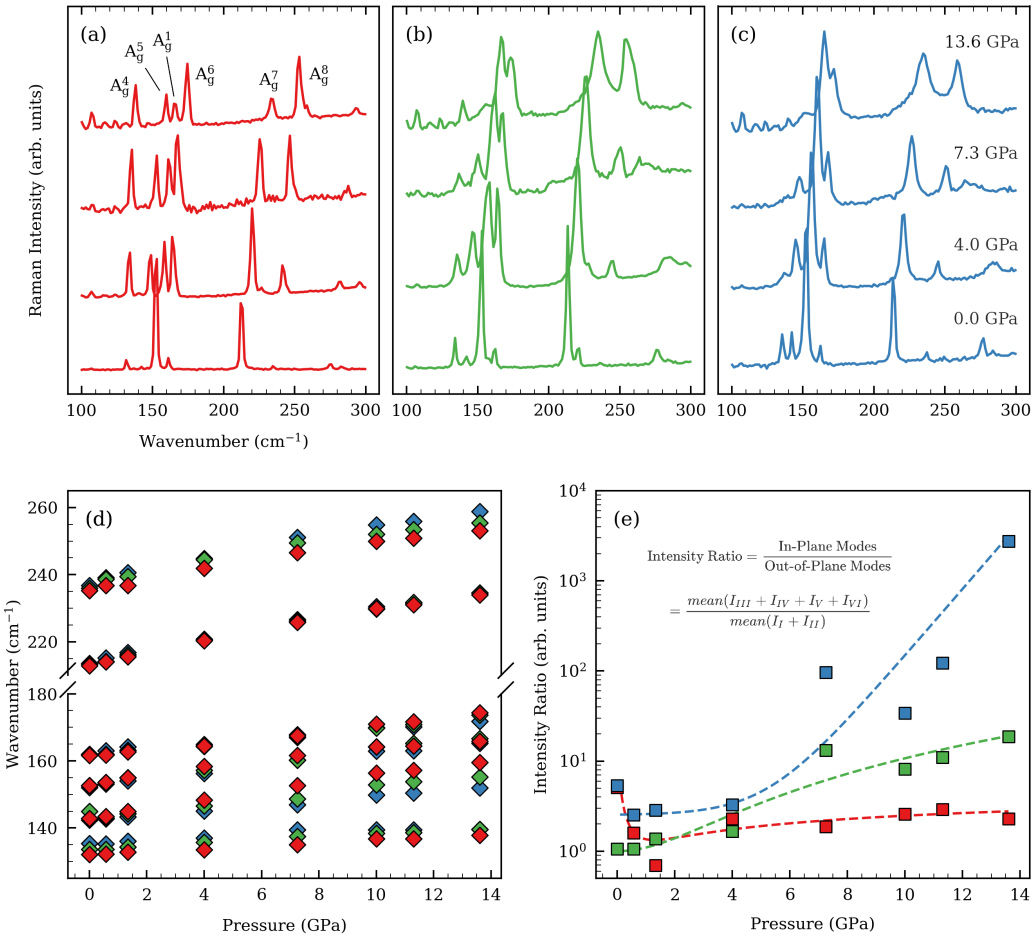

Figure 3.3: Raman spectra of the six lowest-frequency Raman modes of (a) multilayer, (b) bilayer, and (c) monolayer ReS_2 at 0.0, 4.0, 7.3, and 13.6 GPa; (d) Raman shift vs. pressure of the modes shown in (a-c); (e) Intensity ratio on in-plane to out-of-plane Raman modes for each thickness; Dotted lines are shown to guide the eye; Monolayer, bilayer, and multilayer data are shown in blue, green, and red, respectively, throughout.

this transition at ~5 GPa[104], it reportedly does not reach completion in bi- and monolayer samples until 11.9 and 15.4 GPa, respectively[105]. We suggest that this effect is responsible for the stability of multi- and few-layer ReS_2 at higher-than-expected pressures.

3.1.3.1 Vibrational Anisotropy

To study the vibrational anisotropy of ReS_2 under applied compressive strain, we measured the polarized Raman spectra of monolayer and multilayer ReS_2 up to ~12 GPa. Figure 3.4 shows radial plots of the fits to polarized Raman intensities of the A_g^1 (a,d), A_g^6 (b,e), and A_g^8 (c,f) modes at select pressures. Figures A.1 and A.2 show the complete dataset, with experimental data and fits to the data using the Raman tensor of the A_g-type modes of ReS_2, given by:

$$R = \begin{bmatrix} u & v \\ v & w \end{bmatrix} \tag{3.1}$$

with incident and scattered polarization vectors $\hat{e}_i = \hat{e}_s = \begin{bmatrix} \cos\theta & \sin\theta \end{bmatrix}$ for the experimental configuration. Following a similar analysis to that described in Section 2.4.1, the polarization-dependence of the Raman intensity was determined to be:

$$\begin{aligned} I \propto |u|^2 \cos\theta^4 + |w|^2 \sin\theta^4 + 4|v|^2 \cos\theta^2 \sin\theta^2 \\ + 2|u||w| \cos 2\phi_{uw} \cos\theta^2 \sin\theta^2 \\ + 4|u||v| \cos\phi_{uv} \cos\theta^3 \sin\theta \\ + 4|v||w| \cos 2\phi_{vw} \cos\theta \sin\theta^3 \end{aligned} \tag{3.2}$$

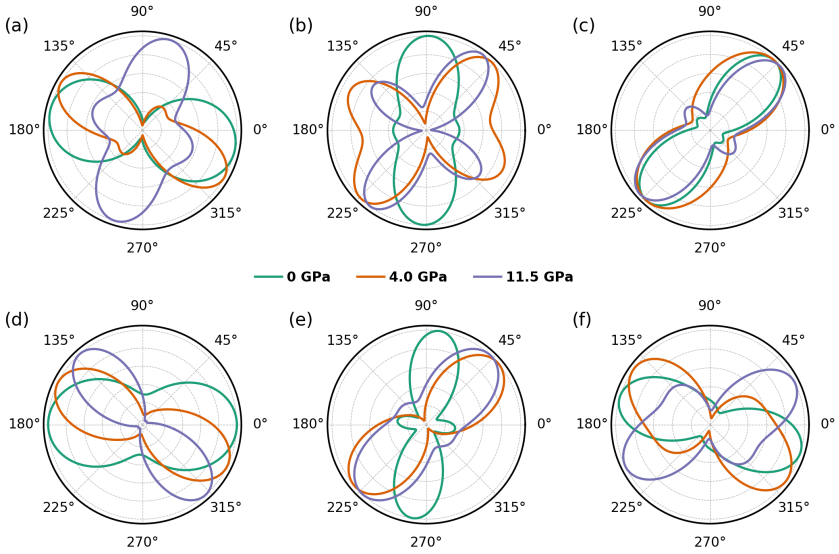

Figure 3.4: Radial plots of showing the evolution of polarized Raman intensities for the (a) A_g^1, (b) A_g^6, and (c) A_g^8 modes of monolayer ReS_2 at various pressures; (d-f) Radial plots of the same mode intensities for multilayer ReS_2.

By fitting Equation 3.2 to experimental data, we were able to determine the Raman tensor elements of ReS_2 for each pressure, the results of which are shown in Figures A.3 and A.4.

3.1.4 Implications for Device Engineering

Comparing ReS_2 with other TMDs, it is clear that the optoelectronic and vibrational properties of ReS_2 are uniquely resilient to strain. Figure 3.5a compares $\Delta E_g/\Delta P$ values extracted from literature data for multilayer MoS_2, $MoSe_2$, WS_2, and WSe_2 (Dybała et al.[106], calculated), multilayer WTe_2 (Lu et al.[107], calculated), monolayer MoS_2 (Nayak et al.[28], experimental), and monolayer WS_2 and $MoWS_2$ (Kim et al.[29], experimental) with the experimental values presented herein. Note that due to the indirect bandgaps of the afore-

mentioned multilayer TMDs, only theoretical optical bandgaps vs. pressure are available. The general trend evident in Figure 3.5a is that compressive strain redshifts bandgaps in multilayer TMDs and blueshifts bandgaps in monolayer TMDs. While ReS_2 is no exception to this trend, both monolayer and multilayer ReS_2 are considerably less sensitive to applied strain than their counterparts, and E_g for bilayer ReS_2 is nearly invariant up to 4 GPa.

The vibrational properties of ReS_2 are similarly robust to applied strain, as is shown in Figure 3.5b. Here, we examine separately the effect of compressive strain on the in-plane vibrational modes (shown as solid-colored bars) and out-of-plane vibrational modes (shown as diagonally hatched bars) of ReS_2, MoS_2[109,28], and WS_2[108,29]. The out-of-plane A' mode of multilayer WS_2, for example, is roughly twice as sensitive to pressure as the in-plane E' mode. This agrees well with the previously mentioned behavior of layered vdW materials, in which higher strain sensitivity in the out-of-plane direction is exhibited by materials with stronger interlayer interactions. In contrast, the out-of-plane modes for mono-, bi-, and multilayer ReS_2 are significantly *less* responsive to strain than their in-plane counterparts: the average $\Delta\omega/\Delta P$ of the out-of-plane A_g^4 and A_g^5 modes for monolayer ReS_2 is only 43% of the in-plane average. For bilayer and multilayer, the same comparison yields values of 54% and 69%, respectively. These results are consistent with the description of multilayer ReS_2 given by Tongay et al.[41], which characterizes the material as consisting of "vibrationally decoupled" monolayers compared with other TMD systems, and clearly demonstrates how that material's weak interlayer interactions scale down to the monolayer limit—a truly layer-decoupled system. We also observe that the out-of-plane modes of monolayer ReS_2 are only ~15% and ~17% as responsive to strain as monolayer WS_2 and MoS_2, respectively, further

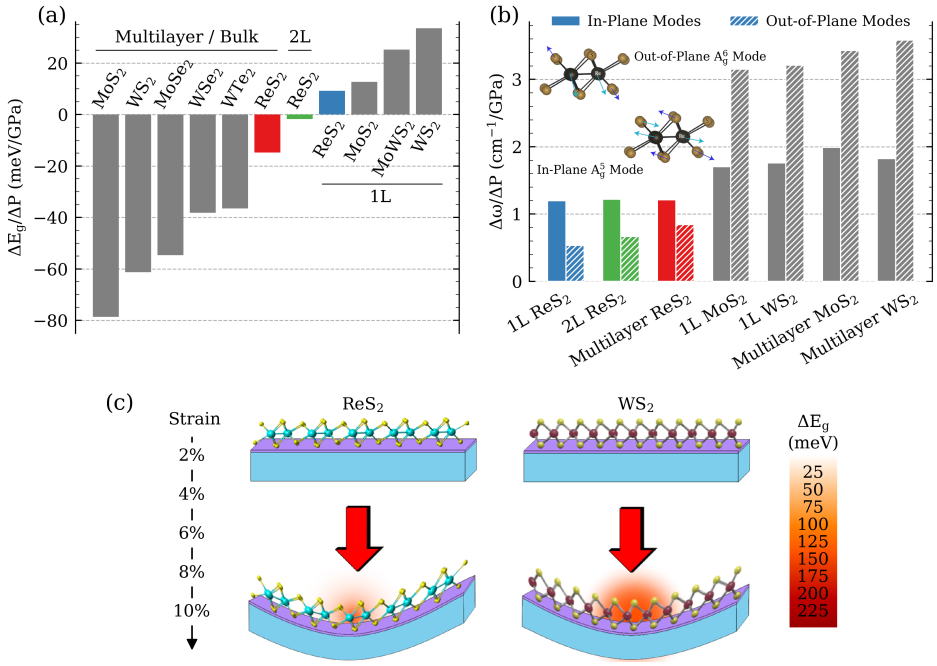

Figure 3.5: (a) Comparison of the bandgap tuning rates between ReS_2 and other mono- and multilayer transition metal dichalcogenides (TMDs); tuning rates were determined by linear fits to E_g vs. pressure data in a limited pressure range below ~10 GPa; the tuning rates for monolayer literature data were obtained from fits to Nayak et al.[28] (MoS_2) and Kim et al.[29] ($MoWS_2$ and WS_2), and multilayer data from fits to calculations by Lu et al.[107] (WTe_2) and Dybała et al.[106] (MoS_2, WS_2, $MoSe_2$, WSe_2). (b) Comparison of Raman mode hardening between in-plane and out-of-plane modes under pressure; our results for ReS_2 are compared with literature values for MoS_2 and WS_2 obtained from fits to Nayak et al.[28,108], Kim et al.[29], and Bandaru et al.[109]; in-plane and out-of-plane modes for MoS_2 are E_{2g} and A_{1g}, respectively, and E' and A' for WS_2; for ReS_2, the values shown are averages of the intensities of the in-plane A_g^1, A_g^6, A_g^7, and A_g^8 modes and the out-of-plane A_g^4 and A_g^4 modes. (c) Illustration of strain tuning in monolayer ReS_2 and WS_2 devices, of which the former offers resilience of electronic and vibrational properties to applied strain and the latter sensitivity—both useful paradigms for engineering flexible electronic devices.

highlighting ReS_2's remarkable strain insensitivity.

The unusually resilient strain-response of ReS_2 should not be overlooked. In device engineering, it is certainly desirable to have direct control over material properties via strain, and the volume of research and interest in strain-sensitive materials such as MoS_2 and WS_2 is a testament to this. However, the opposite paradigm is just as important: for device applications in which maintaining certain electronic properties under rigorous strain is paramount—foldable tablets or surface contouring wearable devices, for example—a strain-resilient semiconductor such as ReS_2 is essential. Figure 3.5c illustrates how these different, but equally important approaches play out in the case of bendable device (a practical analogue to the type of compressive strain described in this work), demonstrating how the bandgaps of ReS_2 and WS_2 might respond under the same applied strain.

3.2 High-Pressure Studies of Black Phosphorus

3.2.1 Electronic and Structural Transitions

Under pressure, the orthorhombic A17 phase of black phosphorus transforms to the rhombohedral A7 phase around 4.5 GPa, followed by the simple cubic (sc) phase above 10.5 GPa. However, recent studies have suggested that there may be an intermediate phase between the A7 and sc phases that persists up to at least 30 GPa[104]. This question is of significance for black phosphorus because the sc phase is superconducting at low temperatures, for which an anomalous pressure evolution of T_c has been observed[110] around 30 GPa. It is possible then that this intermediate phase, which Scelta et al.[104] refer to as the pseudo-simple cubic (p-sc) phase, may provide some insight on superconductivity in BP.

Scelta et al.[104] studies BP up to 30 GPa, and did not explicitly observe a transition from the p-sc to sc phase in that pressure range. Moreover, previous high-pressure Raman studies of the material have not gone above ~25 GPa and offer some conflicting results[111,105,112]. To attempt to resolve this, we have conducted Raman and XRD studies up to 60 GPa in a DAC. Figure 3.6 shows our results alongside those of previous studies. Taking advantage of polarized measurements, we are able to resolve several unassigned peaks that emerge above 10 GPa, which corresponds to the A7 to p-sc transition. In agreement with previous studies, the observation of Raman modes here would suggest that the material is indeed not in the sc phase, for which no Raman-active modes should be present. However, it has not been ruled out that the signals observed are due to other effects. Above 25 GPa, the observed modes become a broad band that rapidly redshifts until the signal disappears above 35 GPa. While by no means conclusive, the dramatic redshift of Raman modes can indicate a structural instability and potential phase transition.

To further investigate the p-sc to sc transition, we recently conducted high-pressure XRD experiments up to 60 GPa. Analysis of these results is still ongoing, but a raw pressure series is shown in Figure 3.7. Peak indexing, structural refinements, and equation-of-state fitting are underway to determine the high-pressure phases. We are optimistic that, taken together, our high-pressure Raman and XRD results will offer new insight into this newly proposed phase and its implications for superconductivity in high-pressure phosphorus.

Black phosphorus also reportedly undergoes an electronic topological transition (ETT) at ~1.2 GPa[113,112]. It has previously been reported that Raman measurements are sensitive to the ETT in BP, since the width of Raman peaks are proportional to the electron-phonon coupling, λ_{qv}[112]. We

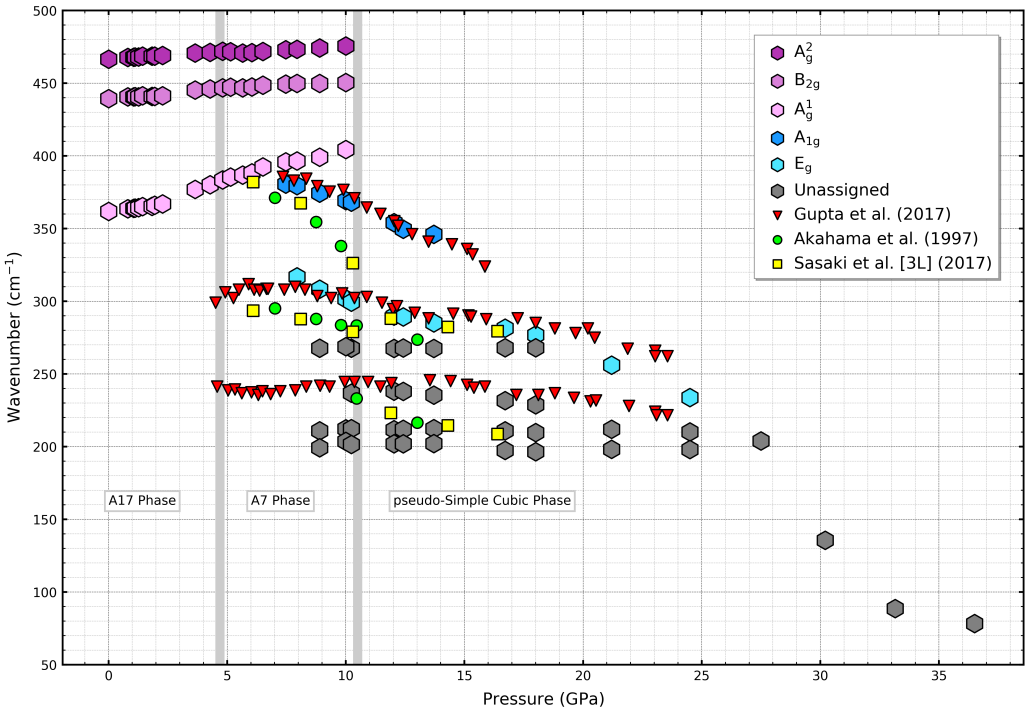

Figure 3.6: Raman shift as a function of pressure for multilayer black phosphorus up ~37 GPa; Data for the characteristic A_g^1, B_{2g}, and A_g^2 modes of the A17 phase are shown as purple octagons; the A_{1g} and E_g modes of the A7 phase are shown as blue octagons; and unidentified modes that persist in the pseudo-simple cubic phase are shown as gray octagons; Literature data are shown for comparison[111,112,105].

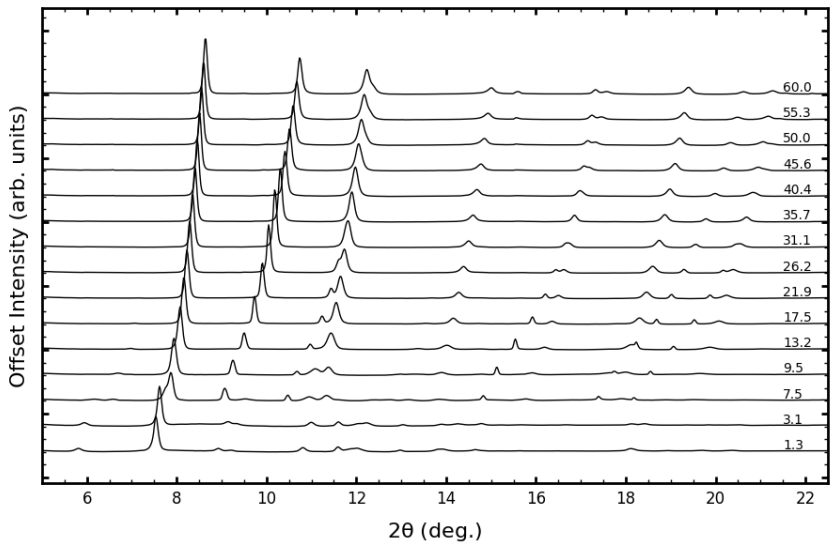

Figure 3.7: Powder x-ray diffraction spectra of bulk black phosphorus up to 60 GPa.

expect that polarized Raman measurements are sensitive to such transitions as well, since the Raman tensor elements are related to the dielectric properties of the crystal (see Equation 2.2). In our high-pressure polarized Raman measurements, we indeed observe that there are noticeable changes to the Raman tensor elements of the B_{2g} and A_g-type modes around the ETT and structural transitions (Figures 3.8 and 3.9). These results suggest that polarized could be used to detect the changes in dielectric properties of materials that accompany both electronic and structural phase transitions. Future theoretical work will be necessary to determine the precise mechanism at play, but our initial results encourage further investigation.

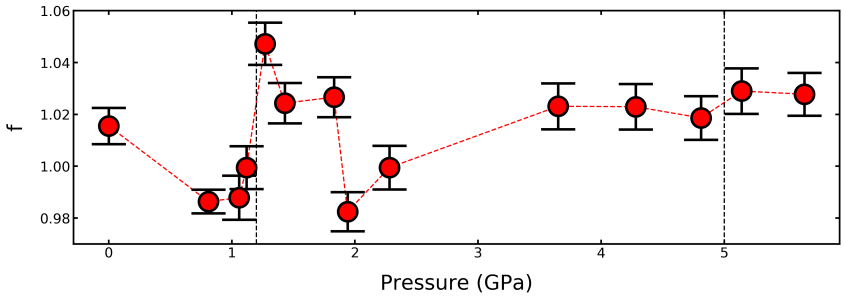

Figure 3.8: Value of the Raman tensor element f for multilayer black phosphorus across the electronic topological phase transition at ~1.2 GPa and the expected structural transition to the A7 phase at ~5 GPa.

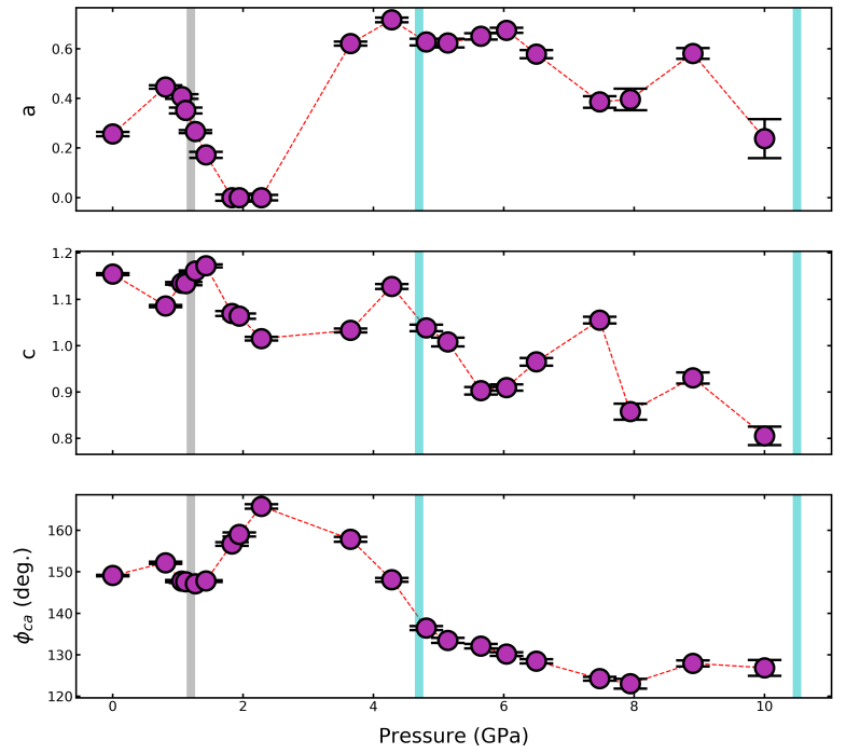

Figure 3.9: Value of the Raman tensor elements $|a|$, $|c|$, and ϕ_{ca} for multilayer black phosphorus across the electronic topological phase transition at ~1.2 GPa and the expected structural transition to the A7 phase at ~5 GPa.

Appendix

Appendix A

Supplemental Figures

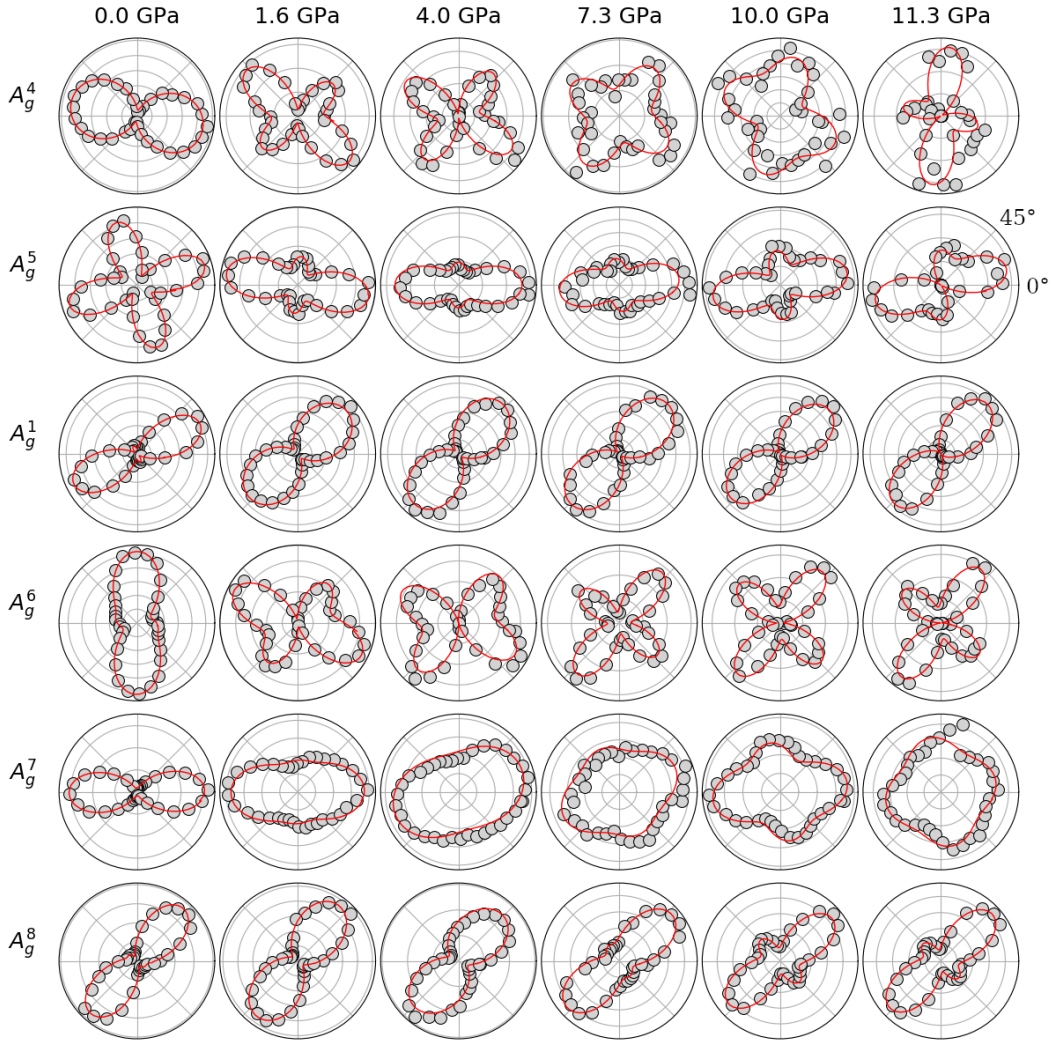

Figure A.1: Radial plots of polarized Raman intensity for monolayer ReS_2; Each plot corresponds to a particular mode and pressure, as indicated on the corresponding axis; Data were collected every 10° over a full 360° rotation, where 0° indicates incident polarization parallel to the $\vec{b}$-axis of the material; Gray circles are experimental data and red lines are fits using the Raman tensor.

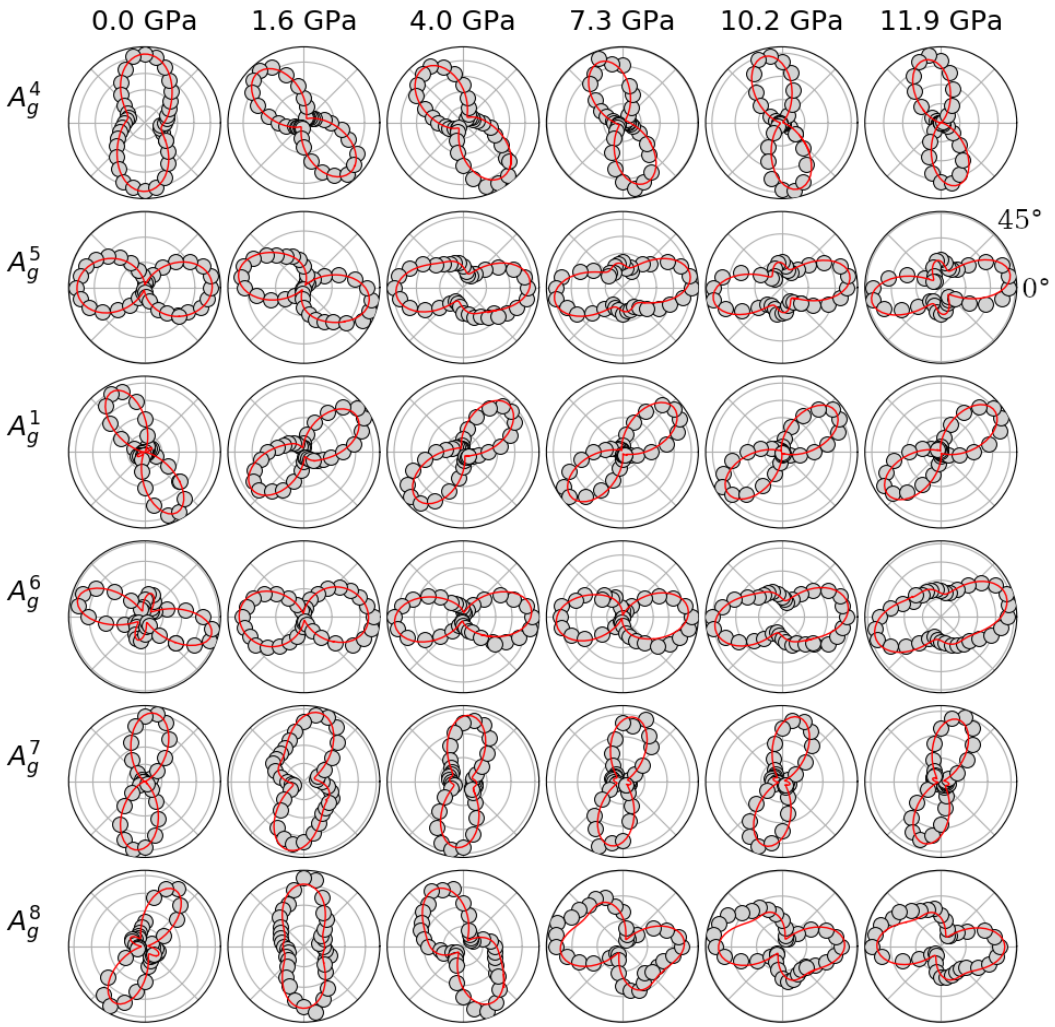

Figure A.2: Radial plots of fits to polarized Raman data for multilayer ReS_2; Each plot corresponds to a particular mode and pressure, as indicated on the corresponding axis; Data were collected every 10° over a full 360° rotation, where 0° indicates incident polarization parallel to the $\vec{b}$-axis of the material; Gray circles are experimental data and red lines are fits using the Raman tensor.

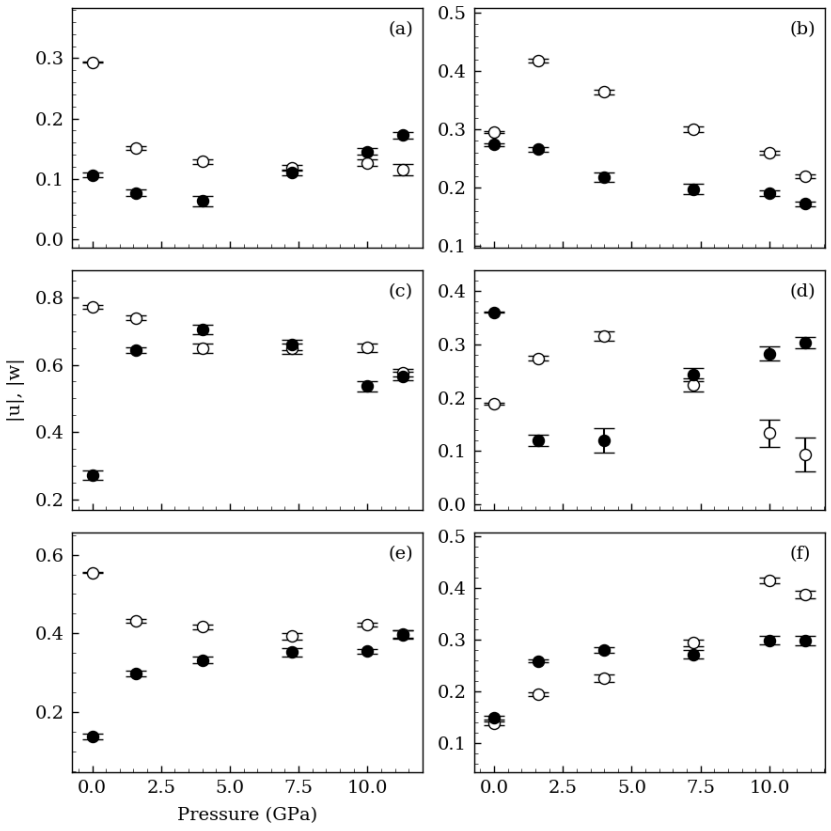

Figure A.3: Raman tensor elements $|u|$ (white circles) and $|w|$ (black circles) as a function of pressure for the six lowest-frequency Raman modes (a-f): A_g^4, A_g^5, A_g^1, A_g^6, A_g^7, and A_g^8.

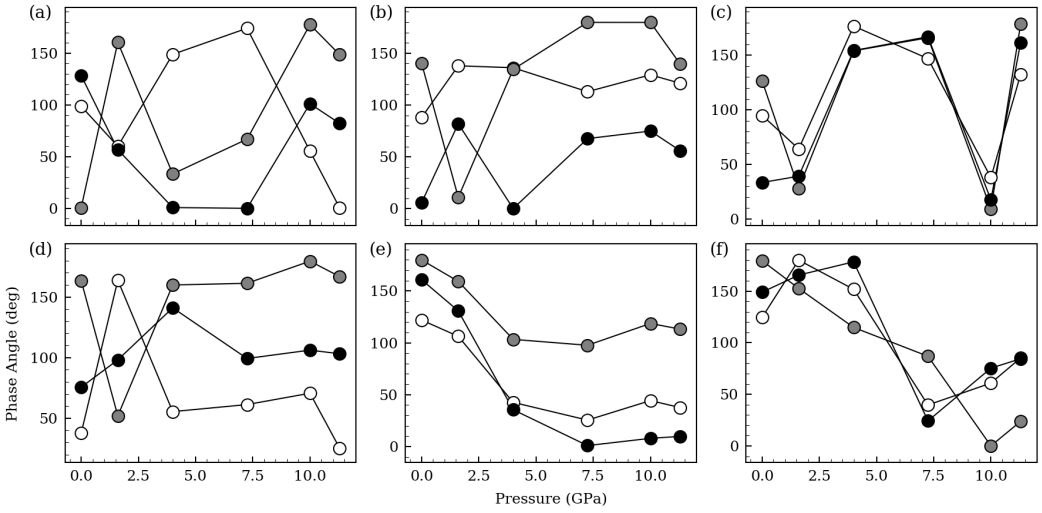

Figure A.4: Raman tensor elements ϕ_u (white circles), ϕ_v (gray circles), ϕ_w (black circles) as a function of pressure for the six lowest-frequency Raman modes (a-f): A_g^4, A_g^5, A_g^1, A_g^6, A_g^7, and A_g^8.

Bibliography

[1] G. H. Olsen, C. J. Nuese, and R. T. Smith. The effect of elastic strain on energy band gap and lattice parameter in III-V compounds. *Journal of Applied Physics*, 49(11):5523–5529, November 1978. ISSN 0021-8979, 1089-7550. doi: 10.1063/1.324472. URL `http://aip.scitation.org/doi/10.1063/1.324472`.

[2] Chris G. Van de Walle. Band lineups and deformation potentials in the model-solid theory. *Physical Review B*, 39(3):1871–1883, January 1989. ISSN 0163-1829. doi: 10.1103/PhysRevB.39.1871. URL `https://link.aps.org/doi/10.1103/PhysRevB.39.1871`.

[3] G. C. Osbourn. Strained-layer superlattices from lattice mismatched materials. *Journal of Applied Physics*, 53(3):1586–1589, March 1982. ISSN 0021-8979, 1089-7550. doi: 10.1063/1.330615. URL `http://aip.scitation.org/doi/10.1063/1.330615`.

[4] C. P. Kuo, S. K. Vong, R. M. Cohen, and G. B. Stringfellow. Effect of mismatch strain on band gap in III-V semiconductors. *Journal of Applied Physics*, 57(12):5428–5432, June 1985. ISSN 0021-8979, 1089-7550. doi: 10.1063/1.334817. URL `http://aip.scitation.org/doi/10.1063/1.334817`.

[5] K. Hung, Y. T. Zhang, and B. Tai. Wearable medical devices for tele-home healthcare. In *The 26th Annual International Conference of the IEEE Engineering in Medicine and Biology Society*, volume 2, pages 5384–5387, September 2004. doi: 10.1109/IEMBS.2004.1404503.

[6] Shideh Kabiri Ameri, Rebecca Ho, Hongwoo Jang, Li Tao, Youhua Wang, Liu Wang, David M. Schnyer, Deji Akinwande, and Nanshu Lu. Graphene Electronic Tattoo Sensors. *ACS Nano*, 11(8):7634–7641, August 2017. ISSN 1936-0851, 1936-086X. doi: 10.1021/acsnano.7b02182. URL `http://pubs.acs.org/doi/10.1021/acsnano.7b02182`.

[7] Mario Pagliaro, Rosaria Ciriminna, and Giovanni Palmisano. Flexible Solar Cells. *ChemSusChem*, 1(11):880–891, November 2008. ISSN 18645631, 1864564X. doi: 10.1002/cssc.200800127. URL http://doi.wiley.com/10.1002/cssc.200800127.

[8] Sangchul Lee, Jun-Seok Yeo, Yongsung Ji, Chunhum Cho, Dong-Yu Kim, Seok-In Na, Byoung Hun Lee, and Takhee Lee. Flexible organic solar cells composed of P3ht:PCBM using chemically doped graphene electrodes. *Nanotechnology*, 23(34):344013, August 2012. ISSN 0957-4484, 1361-6528. doi: 10.1088/0957-4484/23/34/344013. URL http://stacks.iop.org/0957-4484/23/i=34/a=344013?key=crossref.0492440a76140d76d501220ae16a5856.

[9] Andreas Pospischil, Marco M. Furchi, and Thomas Mueller. Solar-energy conversion and light emission in an atomic monolayer p–n diode. *Nature Nanotechnology*, 9(4):257–261, April 2014. ISSN 1748-3387, 1748-3395. doi: 10.1038/nnano.2014.14. URL http://www.nature.com/articles/nnano.2014.14.

[10] Jay Lewis. Material challenge for flexible organic devices. *Materials Today*, 9(4):38–45, April 2006. ISSN 13697021. doi: 10.1016/S1369-7021(06)71446-8. URL https://linkinghub.elsevier.com/retrieve/pii/S1369702106714468.

[11] Myeon-Cheon Choi, Youngkyoo Kim, and Chang-Sik Ha. Polymers for flexible displays: From material selection to device applications. *Progress in Polymer Science*, 33(6):581–630, June 2008. ISSN 00796700. doi: 10.1016/j.progpolymsci.2007.11.004. URL https://linkinghub.elsevier.com/retrieve/pii/S0079670008000105.

[12] Leif Nyholm, Gustav Nyström, Albert Mihranyan, and Maria Strømme. Toward Flexible Polymer and Paper-Based Energy Storage Devices. *Advanced Materials*, pages n/a–n/a, February 2011. ISSN 09359648. doi: 10.1002/adma.201004134. URL http://doi.wiley.com/10.1002/adma.201004134.

[13] You Seung Rim, Sang-Hoon Bae, Huajun Chen, Nicholas De Marco, and Yang Yang. Recent Progress in Materials and Devices toward Printable and Flexible Sensors. *Advanced Materials*, 28(22):4415–4440, June 2016. ISSN 09359648. doi: 10.1002/adma.201505118. URL http://doi.wiley.com/10.1002/adma.201505118.

[14] Zhihao Yu, Zhun-Yong Ong, Songlin Li, Jian-Bin Xu, Gang Zhang, Yong-Wei Zhang, Yi Shi, and Xinran Wang. Analyzing the Carrier Mobility in Transition-Metal Dichalcogenide MoS $_2$ Field-Effect Transistors. *Advanced Functional Materials*, 27(19):1604093, May 2017. ISSN 1616301X. doi: 10.1002/adfm.201604093. URL http://doi.wiley.com/10.1002/adfm.201604093.

[15] Manish Chhowalla, Hyeon Suk Shin, Goki Eda, Lain-Jong Li, Kian Ping Loh, and Hua Zhang. The chemistry of two-dimensional layered transition metal dichalcogenide nanosheets. *Nature Chemistry*, 5(4):263–275, April 2013. ISSN 1755-4330, 1755-4349. doi: 10.1038/nchem.1589. URL http://www.nature.com/articles/nchem.1589.

[16] Jun Kang, Sefaattin Tongay, Jian Zhou, Jingbo Li, and Junqiao Wu. Band offsets and heterostructures of two-dimensional semiconductors. *Applied Physics Letters*, 102(1):012111, January 2013. ISSN 0003-6951, 1077-3118. doi: 10.1063/1.4774090. URL http://aip.scitation.org/doi/10.1063/1.4774090.

[17] B. Radisavljevic, A. Radenovic, J. Brivio, V. Giacometti, and A. Kis. Single-layer MoS2 transistors. *Nature Nanotechnology*, 6(3):147–150, March 2011. ISSN 1748-3387, 1748-3395. doi: 10.1038/nnano.2010.279. URL http://www.nature.com/articles/nnano.2010.279.

[18] Xiaodong Li, Jeffrey T. Mullen, Zhenghe Jin, Kostyantyn M. Borysenko, M. Buongiorno Nardelli, and Ki Wook Kim. Intrinsic electrical transport properties of monolayer silicene and MoS 2 from first principles. *Physical Review B*, 87(11):115418, March 2013. ISSN 1098-0121, 1550-235X. doi: 10.1103/PhysRevB.87.115418. URL https://link.aps.org/doi/10.1103/PhysRevB.87.115418.

[19] Deji Akinwande, Nicholas Petrone, and James Hone. Two-dimensional flexible nanoelectronics. *Nature Communications*, 5(1), December 2014. ISSN 2041-1723. doi: 10.1038/ncomms6678. URL http://www.nature.com/articles/ncomms6678.

[20] Keliang He, Charles Poole, Kin Fai Mak, and Jie Shan. Experimental Demonstration of Continuous Electronic Structure Tuning via Strain in Atomically Thin MoS $_2$. *Nano Letters*, 13(6):2931–2936, June 2013. ISSN 1530-6984, 1530-6992. doi: 10.1021/nl4013166. URL http://pubs.acs.org/doi/10.1021/nl4013166.

[21] Hongliang Shi, Hui Pan, Yong-Wei Zhang, and Boris I. Yakobson. Quasiparticle band structures and optical properties of strained monolayer MoS 2 and WS 2. *Physical Review B*, 87(15):155304, April 2013. ISSN 1098-0121, 1550-235X. doi: 10.1103/PhysRevB.87.155304. URL https://link.aps.org/doi/10.1103/PhysRevB.87.155304.

[22] M. Ghorbani-Asl, S. Borini, A. Kuc, and T. Heine. Strain-dependent modulation of conductivity in single-layer transition-metal dichalcogenides. *Physical Review B*, 87(23):235434, June 2013. ISSN 1098-0121, 1550-235X. doi: 10.1103/PhysRevB.87.235434. URL https://link.aps.org/doi/10.1103/PhysRevB.87.235434.

[23] Yanlong Wang, Chunxiao Cong, Weihuang Yang, Jingzhi Shang, Namphung Peimyoo, Yu Chen, Junyong Kang, Jianpu Wang, Wei Huang, and Ting Yu. Strain-induced direct–indirect bandgap transition and phonon modulation in monolayer WS2. *Nano Research*, 8(8):2562–2572, August 2015. ISSN 1998-0124, 1998-0000. doi: 10.1007/s12274-015-0762-6. URL http://link.springer.com/10.1007/s12274-015-0762-6.

[24] Aamir Shafique and Young-Han Shin. Strain engineering of phonon thermal transport properties in monolayer 2h-MoTe $_2$. *Physical Chemistry Chemical Physics*, 19(47):32072–32078, 2017. ISSN 1463-9076, 1463-9084. doi: 10.1039/C7CP06065C. URL http://xlink.rsc.org/?DOI=C7CP06065C.

[25] Do Muoi, Nguyen N. Hieu, Huong T.T. Phung, Huynh V. Phuc, B. Amin, Bui D. Hoi, Nguyen V. Hieu, Le C. Nhan, Chuong V. Nguyen, and P.T.T. Le. Electronic properties of WS2 and WSe2 monolayers with biaxial strain: A first-principles study. *Chemical Physics*, 519:69–73, March 2019. ISSN 03010104. doi: 10.1016/j.chemphys.2018.12.004. URL https://linkinghub.elsevier.com/retrieve/pii/S0301010418312904.

[26] Dimple, Nityasagar Jena, and Abir De Sarkar. Compressive strain induced enhancement in thermoelectric power factor in monolayer mos2 nanosheet. *Journal of Physics: Condensed Matter*, 29(22): 225501, June 2017. ISSN 0953-8984, 1361-648X. doi: 10.1088/1361-648X/aa6cbc. URL http://stacks.iop.org/0953-8984/29/i=22/a=225501?key=crossref.fdf37bb955bd63609465c6ce68d76521.

[27] Xiuming Dou, Kun Ding, Desheng Jiang, and Baoquan Sun. Tuning and Identification of Interband Transitions in Monolayer and Bilayer Molybdenum Disulfide Using Hydrostatic Pressure. *ACS Nano*, 8(7):7458–7464, July 2014. ISSN 1936-0851, 1936-086X. doi: 10.1021/nn502717d. URL http://pubs.acs.org/doi/10.1021/nn502717d.

[28] Avinash P. Nayak, Tribhuwan Pandey, Damien Voiry, Jin Liu, Samuel T. Moran, Ankit Sharma, Cheng Tan, Chang-Hsiao Chen, Lain-Jong Li, Manish Chhowalla, Jung-Fu Lin, Abhishek K. Singh, and Deji Akinwande. Pressure-Dependent Optical and Vibrational Properties of Monolayer Molybdenum Disulfide. *Nano Letters*, 15(1):346–353, January 2015. ISSN 1530-6984, 1530-6992. doi: 10.1021/nl5036397. URL http://pubs.acs.org/doi/10.1021/nl5036397.

[29] Joon-Seok Kim, Rafia Ahmad, Tribhuwan Pandey, Amritesh Rai, Simin Feng, Jing Yang, Zhong Lin, Mauricio Terrones, Sanjay K Banerjee, Abhishek K Singh, Deji Akinwande, and Jung-Fu Lin. Towards band structure and band offset engineering of monolayer $Mo_{(1-x)}W_{(x)}S_2$ via strain. *2D Materials*, 5(1):015008, October 2017. ISSN 2053-1583. doi: 10.1088/2053-1583/aa8e71. URL http://stacks.iop.org/2053-1583/5/i=1/a=015008?key=crossref.d1fc82e3b9d7b6564531213aa2cd8ca1.

[30] Yabin Chen, Feng Ke, Penghong Ci, Changhyun Ko, Taegyun Park, Sahar Saremi, Huili Liu, Yeonbae Lee, Joonki Suh, Lane W. Martin, Joel W. Ager, Bin Chen, and Junqiao Wu. Pressurizing Field-Effect Transistors of Few-Layer MoS $_2$ in a Diamond Anvil Cell. *Nano Letters*, 17(1):194–199, January 2017. ISSN 1530-6984, 1530-6992. doi: 10.1021/acs.nanolett.6b03785. URL http://pubs.acs.org/doi/10.1021/acs.nanolett.6b03785.

[31] Munkhbayar Batmunkh, Munkhjargal Bat-Erdene, and Joseph G. Shapter. Phosphorene and Phosphorene-Based Materials - Prospects for Future Applications. *Advanced Materials*, 28(39):8586–8617, October 2016. ISSN 09359648. doi: 10.1002/adma.201602254. URL http://doi.wiley.com/10.1002/adma.201602254.

[32] Fucai Liu, Shoujun Zheng, Xuexia He, Apoorva Chaturvedi, Junfeng He, Wai Leong Chow, Thomas R. Mion, Xingli Wang, Jiadong Zhou, Qundong Fu, Hong Jin Fan, Beng Kang Tay, Li Song, Rui-Hua He, Christian Kloc, Pulickel M. Ajayan, and Zheng Liu. Highly Sensitive Detection of Polarized Light Using Anisotropic 2d ReS $_2$. *Advanced Functional Materials*, 26(8):1169–1177, February 2016. ISSN 1616301X. doi: 10.1002/adfm.201504546. URL http://doi.wiley.com/10.1002/adfm.201504546.

[33] Lei Ye, Peng Wang, Wenjin Luo, Fan Gong, Lei Liao, Tiande Liu, Lei Tong, Jianfeng Zang, Jianbin Xu, and Weida Hu. Highly polarization sensitive infrared photodetector based on black phosphorus-on-WSe 2 photogate vertical heterostructure. *Nano Energy*, 37:53–60, July 2017. ISSN 22112855. doi: 10.1016/j.nanoen.2017.05.004. URL https://linkinghub.elsevier.com/retrieve/pii/S2211285517302781.

[34] Andres Castellanos-Gomez. Black Phosphorus: Narrow Gap, Wide Applications. *The Journal of Physical Chemistry Letters*, 6(21):4280–4291, November 2015. ISSN 1948-7185. doi: 10.1021/acs.jpclett.5b01686. URL http://pubs.acs.org/doi/10.1021/acs.jpclett.5b01686.

[35] Yu Zhang, Yun Zheng, Kun Rui, Huey Hoon Hng, Kedar Hippalgaonkar, Jianwei Xu, Wenping Sun, Jixin Zhu, Qingyu Yan, and Wei Huang. 2d

Black Phosphorus for Energy Storage and Thermoelectric Applications. *Small*, 13(28):1700661, July 2017. ISSN 16136810. doi: 10.1002/smll.201700661. URL http://doi.wiley.com/10.1002/smll.201700661.

[36] Qin Zhang, Shuangjie Tan, Rafael G. Mendes, Zhongti Sun, Yongting Chen, Xin Kong, Yinghui Xue, Mark H. Rümmeli, Xiaojun Wu, Shengli Chen, and Lei Fu. Extremely Weak van der Waals Coupling in Vertical ReS2 Nanowalls for High-Current-Density Lithium-Ion Batteries. *Advanced Materials*, 28(13):2616–2623, 2016. ISSN 1521-4095. doi: 10.1002/adma.201505498. URL http://onlinelibrary.wiley.com/doi/abs/10.1002/adma.201505498.

[37] Huimei Liu, Bo Xu, J.-M. Liu, Jiang Yin, Feng Miao, Chun-Gang Duan, and X. G. Wan. Highly efficient and ultrastable visible-light photocatalytic water splitting over ReS $_2$. *Physical Chemistry Chemical Physics*, 18(21):14222–14227, 2016. ISSN 1463-9076, 1463-9084. doi: 10.1039/C6CP01007E. URL http://xlink.rsc.org/?DOI=C6CP01007E.

[38] Jianwen Huang, Haigen Gao, Yufei Xia, Yinghui Sun, Jie Xiong, Yanrong Li, Shan Cong, Jun Guo, Shiyu Du, and Guifu Zou. Enhanced photoelectrochemical performance of defect-rich ReS2 nanosheets in visible-light assisted hydrogen generation. *Nano Energy*, 46:305–313, April 2018. ISSN 2211-2855. doi: 10.1016/j.nanoen.2018.02.003. URL http://www.sciencedirect.com/science/article/pii/S2211285518300648.

[39] Xiaoyong Xu, Heng Zhao, Rui Wang, Zehui Zhang, Xuefeng Dong, Jing Pan, Jingguo Hu, and Haibo Zeng. Identification of few-layer ReS2 as photo-electro integrated catalyst for hydrogen evolution. *Nano Energy*, 48:337–344, June 2018. ISSN 2211-2855. doi: 10.1016/j.nanoen.2018.03.078. URL http://www.sciencedirect.com/science/article/pii/S2211285518302209.

[40] Qihua Jing, Hao Zhang, Hao Huang, Xingce Fan, Yumeng Zhang, Xiangyu Hou, Qingyu Xu, Zhenhua Ni, and Teng Qiu. Ultrasonic exfoliated ReS $_2$ nanosheets: fabrication and use as co-catalyst for enhancing photocatalytic efficiency of TiO $_2$ nanoparticles under sunlight. *Nanotechnology*, 30(18):184001, May 2019. ISSN 0957-4484, 1361-6528.

doi: 10.1088/1361-6528/ab00b4. URL https://iopscience.iop.org/article/10.1088/1361-6528/ab00b4.

[41] Sefaattin Tongay, Hasan Sahin, Changhyun Ko, Alex Luce, Wen Fan, Kai Liu, Jian Zhou, Ying-Sheng Huang, Ching-Hwa Ho, Jinyuan Yan, D. Frank Ogletree, Shaul Aloni, Jie Ji, Shushen Li, Jingbo Li, F. M. Peeters, and Junqiao Wu. Monolayer behaviour in bulk ReS2 due to electronic and vibrational decoupling. *Nature Communications*, 5(1), December 2014. ISSN 2041-1723. doi: 10.1038/ncomms4252. URL http://www.nature.com/articles/ncomms4252.

[42] Ankit Jain and Alan J. H. McGaughey. Strongly anisotropic in-plane thermal transport in single-layer black phosphorene. *Scientific Reports*, 5(1), July 2015. ISSN 2045-2322. doi: 10.1038/srep08501. URL http://www.nature.com/articles/srep08501.

[43] Huili Liu, Hwan Sung Choe, Yabin Chen, Joonki Suh, Changhyun Ko, Sefaattin Tongay, and Junqiao Wu. Variable range hopping electric and thermoelectric transport in anisotropic black phosphorus. *Applied Physics Letters*, 111(10):102101, September 2017. ISSN 0003-6951, 1077-3118. doi: 10.1063/1.4985333. URL http://aip.scitation.org/doi/10.1063/1.4985333.

[44] K. S. Novoselov. Electric Field Effect in Atomically Thin Carbon Films. *Science*, 306(5696):666–669, October 2004. ISSN 0036-8075, 1095-9203. doi: 10.1126/science.1102896. URL http://www.sciencemag.org/cgi/doi/10.1126/science.1102896.

[45] K. S. Novoselov, A. K. Geim, S. V. Morozov, D. Jiang, M. I. Katsnelson, I. V. Grigorieva, S. V. Dubonos, and A. A. Firsov. Two-dimensional gas of massless Dirac fermions in graphene. *Nature*, 438(7065):197–200, November 2005. ISSN 0028-0836, 1476-4687. doi: 10.1038/nature04233. URL http://www.nature.com/articles/nature04233.

[46] Joon-Seok Kim, Yingnan Liu, Weinan Zhu, Seohee Kim, Di Wu, Li Tao, Ananth Dodabalapur, Keji Lai, and Deji Akinwande. Toward air-stable multilayer phosphorene thin-films and transistors. *Scientific Reports*,

5(1), August 2015. ISSN 2045-2322. doi: 10.1038/srep08989. URL http://www.nature.com/articles/srep08989.

[47] Kyounghwan Kim, Matthew Yankowitz, Babak Fallahazad, Sangwoo Kang, Hema C. P. Movva, Shengqiang Huang, Stefano Larentis, Chris M. Corbet, Takashi Taniguchi, Kenji Watanabe, Sanjay K. Banerjee, Brian J. LeRoy, and Emanuel Tutuc. van der Waals Heterostructures with High Accuracy Rotational Alignment. *Nano Letters*, 16(3):1989–1995, March 2016. ISSN 1530-6984, 1530-6992. doi: 10.1021/acs.nanolett.5b05263. URL http://pubs.acs.org/doi/10.1021/acs.nanolett.5b05263.

[48] Ozgur Burak Aslan, Daniel A. Chenet, Arend M. van der Zande, James C. Hone, and Tony F. Heinz. Linearly Polarized Excitons in Single- and Few-Layer ReS $_2$ Crystals. *ACS Photonics*, 3(1):96–101, January 2016. ISSN 2330-4022, 2330-4022. doi: 10.1021/acsphotonics.5b00486. URL http://pubs.acs.org/doi/10.1021/acsphotonics.5b00486.

[49] Xiao-Fen Qiao, Jiang-Bin Wu, Linwei Zhou, Jingsi Qiao, Wei Shi, Tao Chen, Xin Zhang, Jun Zhang, Wei Ji, and Ping-Heng Tan. Polytypism and unexpected strong interlayer coupling in two-dimensional layered ReS $_2$. *Nanoscale*, 8(15):8324–8332, 2016. ISSN 2040-3364, 2040-3372. doi: 10.1039/C6NR01569G. URL http://xlink.rsc.org/?DOI=C6NR01569G.

[50] Daniel A. Chenet, O. Burak Aslan, Pinshane Y. Huang, Chris Fan, Arend M. van der Zande, Tony F. Heinz, and James C. Hone. In-Plane Anisotropy in Mono- and Few-Layer ReS $_2$ Probed by Raman Spectroscopy and Scanning Transmission Electron Microscopy. *Nano Letters*, 15(9):5667–5672, September 2015. ISSN 1530-6984, 1530-6992. doi: 10.1021/acs.nanolett.5b00910. URL http://pubs.acs.org/doi/10.1021/acs.nanolett.5b00910.

[51] Amber McCreary, Jeffrey R. Simpson, Yuanxi Wang, Daniel Rhodes, Kazunori Fujisawa, Luis Balicas, Madan Dubey, Vincent H. Crespi, Mauricio Terrones, and Angela R. Hight Walker. Intricate Resonant Raman Response in Anisotropic ReS $_2$. *Nano Letters*, 17(10):5897–5907, October 2017. ISSN 1530-6984, 1530-6992. doi: 10.1021/acs.nanolett.7b01463. URL http://pubs.acs.org/doi/10.1021/acs.nanolett.7b01463.

[52] P. Nemes-Incze, Z. Osváth, K. Kamarás, and L.P. Biró. Anomalies in thickness measurements of graphene and few layer graphite crystals by tapping mode atomic force microscopy. *Carbon*, 46(11):1435–1442, September 2008. ISSN 00086223. doi: 10.1016/j.carbon.2008.06.022. URL http://linkinghub.elsevier.com/retrieve/pii/S0008622308002856.

[53] Cameron J Shearer, Ashley D Slattery, Andrew J Stapleton, Joseph G Shapter, and Christopher T Gibson. Accurate thickness measurement of graphene. *Nanotechnology*, 27(12):125704, March 2016. ISSN 0957-4484, 1361-6528. doi: 10.1088/0957-4484/27/12/125704. URL http://stacks.iop.org/0957-4484/27/i=12/a=125704?key=crossref.bb2344354c7599092255f831e0eb8f63.

[54] Hai Li, Jumiati Wu, Xiao Huang, Gang Lu, Jian Yang, Xin Lu, Qihua Xiong, and Hua Zhang. Rapid and Reliable Thickness Identification of Two-Dimensional Nanosheets Using Optical Microscopy. *ACS Nano*, 7(11):10344–10353, November 2013. ISSN 1936-0851, 1936-086X. doi: 10.1021/nn4047474. URL http://pubs.acs.org/doi/10.1021/nn4047474.

[55] Philip Dalladay-Simpson, Ross T. Howie, and Eugene Gregoryanz. Evidence for a new phase of dense hydrogen above 325 gigapascals. *Nature*, 529(7584):63–67, January 2016. ISSN 0028-0836, 1476-4687. doi: 10.1038/nature16164. URL http://www.nature.com/articles/nature16164.

[56] Ranga P. Dias and Isaac F. Silvera. Observation of the Wigner-Huntington transition to metallic hydrogen. *Science*, 355(6326):715–718, February 2017. ISSN 0036-8075, 1095-9203. doi: 10.1126/science.aal1579. URL http://www.sciencemag.org/lookup/doi/10.1126/science.aal1579.

[57] Alexander F. Goncharov, Sergey S. Lobanov, Xiaojing Tan, Gregory T. Hohensee, David G. Cahill, Jung-Fu Lin, Sylvia-Monique Thomas, Takuo Okuchi, and Naotaka Tomioka. Experimental study of thermal conductivity at high pressures: Implications for the deep Earth's interior. *Physics of the Earth and Planetary Interiors*, 247:11–16, October

2015. ISSN 00319201. doi: 10.1016/j.pepi.2015.02.004. URL https://linkinghub.elsevier.com/retrieve/pii/S0031920115000199.

[58] Suyu Fu, Jing Yang, and Jung-Fu Lin. Abnormal Elasticity of Single-Crystal Magnesiosiderite across the Spin Transition in Earth's Lower Mantle. *Physical Review Letters*, 118(3), January 2017. ISSN 0031-9007, 1079-7114. doi: 10.1103/PhysRevLett.118.036402. URL https://link.aps.org/doi/10.1103/PhysRevLett.118.036402.

[59] Jung-Fu Lin. Melting behavior of H $_2$ O at high pressures and temperatures. *Geophysical Research Letters*, 32(11):L11306, 2005. ISSN 0094-8276. doi: 10.1029/2005GL022499. URL http://doi.wiley.com/10.1029/2005GL022499.

[60] Yuki Asahara, Kei Hirose, Yasuo Ohishi, Naohisa Hirao, and Motohiko Murakami. Thermoelastic properties of ice VII and its high-pressure polymorphs: Implications for dynamics of cold slab subduction in the lower mantle. *Earth and Planetary Science Letters*, 299(3-4):474–482, November 2010. ISSN 0012821X. doi: 10.1016/j.epsl.2010.09.037. URL http://linkinghub.elsevier.com/retrieve/pii/S0012821X10006126.

[61] M. Guthrie, R. Boehler, J. J. Molaison, B. Haberl, A. M. dos Santos, and C. Tulk. Structure and disorder in ice VII on the approach to hydrogen-bond symmetrization. *Physical Review B*, 99(18):184112, May 2019. ISSN 2469-9950, 2469-9969. doi: 10.1103/PhysRevB.99.184112. URL https://link.aps.org/doi/10.1103/PhysRevB.99.184112.

[62] University College London Materials Chemistry Center. Diamond anvil cell, April 2006. URL https://www.ucl.ac.uk/mcc/.

[63] Reinhard Boehler. New diamond cell for single-crystal x-ray diffraction. *Review of Scientific Instruments*, 77(11):115103, November 2006. ISSN 0034-6748, 1089-7623. doi: 10.1063/1.2372734. URL http://aip.scitation.org/doi/10.1063/1.2372734.

[64] R. Boehler, J. J. Molaison, and B. Haberl. Novel diamond cells for neutron diffraction using multi-carat CVD anvils. *Review of Scientific Instruments*, 88(8):083905, August 2017. ISSN 0034-6748, 1089-7623. doi:

10.1063/1.4997265. URL http://aip.scitation.org/doi/10.1063/1.4997265.

[65] Juanxia Wu, Nannan Mao, Liming Xie, Hua Xu, and Jin Zhang. Identifying the Crystalline Orientation of Black Phosphorus Using Angle-Resolved Polarized Raman Spectroscopy. *Angewandte Chemie International Edition*, 54(8):2366–2369, February 2015. ISSN 14337851. doi: 10.1002/anie.201410108. URL http://doi.wiley.com/10.1002/anie.201410108.

[66] Yan Cao, Natalya Sheremetyeva, Liangbo Liang, Hui Yuan, Tingting Zhong, Vincent Meunier, and Minghu Pan. Anomalous vibrational modes in few layer WTe $_2$ revealed by polarized Raman scattering and first-principles calculations. *2D Materials*, 4(3): 035024, August 2017. ISSN 2053-1583. doi: 10.1088/2053-1583/aa7f5a. URL http://stacks.iop.org/2053-1583/4/i=3/a=035024?key=crossref.d2bced86119ef2023342bd1504d26cf1.

[67] Shengxue Yang, Cong Wang, Hasan Sahin, Hui Chen, Yan Li, Shu-Shen Li, Aslihan Suslu, Francois M. Peeters, Qian Liu, Jingbo Li, and Sefaattin Tongay. Tuning the Optical, Magnetic, and Electrical Properties of ReSe $_2$ by Nanoscale Strain Engineering. *Nano Letters*, 15(3):1660–1666, March 2015. ISSN 1530-6984, 1530-6992. doi: 10.1021/nl504276u. URL http://pubs.acs.org/doi/10.1021/nl504276u.

[68] Sangwan Sim, Doeon Lee, Minji Noh, Soonyoung Cha, Chan Ho Soh, Ji Ho Sung, Moon-Ho Jo, and Hyunyong Choi. Selectively tunable optical Stark effect of anisotropic excitons in atomically thin ReS2. *Nature Communications*, 7:13569, November 2016. ISSN 2041-1723. doi: 10.1038/ncomms13569. URL http://www.nature.com/doifinder/10.1038/ncomms13569.

[69] Xianghai Meng, Yongjian Zhou, Ke Chen, Richard H. Roberts, Wenzhi Wu, Jung-Fu Lin, Ray T. Chen, Xiaochuan Xu, and Yaguo Wang. Anisotropic Saturable and Excited-State Absorption in Bulk ReS $_2$. *Advanced Optical Materials*, 6(14):1800137, July 2018. ISSN 21951071. doi: 10.1002/adom.201800137. URL http://doi.wiley.com/10.1002/adom.201800137.

[70] Weinan Zhu, Liangbo Liang, Richard H. Roberts, Jung-Fu Lin, and Deji Akinwande. Anisotropic Electron–Phonon Interactions in Angle-Resolved Raman Study of Strained Black Phosphorus. *ACS Nano*, 12(12):12512–12522, December 2018. ISSN 1936-085O. doi: 10.1021/acsnano.8b06940. URL https://doi.org/10.1021/acsnano.8b06940.

[71] Duhee Yoon, Hyerim Moon, Young-Woo Son, Jin Sik Choi, Bae Ho Park, Young Hun Cha, Young Dong Kim, and Hyeonsik Cheong. Interference effect on Raman spectrum of graphene on SiO 2 / Si. *Physical Review B*, 80(12), September 2009. ISSN 1098-0121, 1550-235X. doi: 10.1103/PhysRevB.80.125422. URL https://link.aps.org/doi/10.1103/PhysRevB.80.125422.

[72] Jungcheol Kim, Jae-Ung Lee, Jinhwan Lee, Hyo Ju Park, Zonghoon Lee, Changgu Lee, and Hyeonsik Cheong. Anomalous polarization dependence of Raman scattering and crystallographic orientation of black phosphorus. *Nanoscale*, 7(44):18708–18715, 2015. ISSN 2040-3364, 2040-3372. doi: 10.1039/C5NR04349B. URL http://xlink.rsc.org/?DOI=C5NR04349B.

[73] R. Rollefson and R. Havens. Index of Refraction of Methane in the Infra-Red and the Dipole Moment of the CH Bond. *Physical Review*, 57 (8):710–717, April 1940. ISSN 0031-899X. doi: 10.1103/PhysRev.57.710. URL https://link.aps.org/doi/10.1103/PhysRev.57.710.

[74] H Asahina and A Morita. Band structure and optical properties of black phosphorus. *Journal of Physics C: Solid State Physics*, 17(11): 1839–1852, April 1984. ISSN 0022-3719. doi: 10.1088/0022-3719/17/11/006. URL http://stacks.iop.org/0022-3719/17/i=11/a=006?key=crossref.fc565e38859c71407d9e449bc9e4da99.

[75] O. S. Heavens. Optical properties of thin films. *Reports on Progress in Physics*, 23(1):1–65, January 1960. ISSN 0034-4885. doi: 10.1088/0034-4885/23/1/301. URL https://doi.org/10.1088%2F0034-4885%2F23%2F1%2F301.

[76] I. H. Malitson. Interspecimen Comparison of the Refractive Index of Fused Silica. *JOSA*, 55(10):1205–1209, October 1965. doi: 10.1364/JOSA.55.

001205. URL https://www.osapublishing.org/josa/abstract.cfm?uri=josa-55-10-1205.

[77] G. Vuye, S. Fisson, V. Nguyen Van, Y. Wang, J. Rivory, and F. Abelès. Temperature dependence of the dielectric function of silicon using in situ spectroscopic ellipsometry. *Thin Solid Films*, 233(1):166–170, October 1993. ISSN 0040-6090. doi: 10.1016/0040-6090(93)90082-Z. URL http://www.sciencedirect.com/science/article/pii/004060909390082Z.

[78] Philipp Nagler, Gerd Plechinger, Christian Schüller, and Tobias Korn. Observation of anisotropic interlayer Raman modes in few-layer ReS 2. *physica status solidi (RRL) - Rapid Research Letters*, 10(2):185–189, February 2016. ISSN 18626254. doi: 10.1002/pssr.201510412. URL http://doi.wiley.com/10.1002/pssr.201510412.

[79] Dawei Zhou, Yonghui Zhou, Chunying Pu, Xuliang Chen, Pengchao Lu, Xuefei Wang, Chao An, Ying Zhou, Feng Miao, Ching-Hwa Ho, Jian Sun, Zhaorong Yang, and Dingyu Xing. Pressure-induced metallization and superconducting phase in ReS 2. *npj Quantum Materials*, 2(1), December 2017. ISSN 2397-4648. doi: 10.1038/s41535-017-0023-x. URL http://www.nature.com/articles/s41535-017-0023-x.

[80] Yung-Chang Lin, Hannu-Pekka Komsa, Chao-Hui Yeh, Torbjörn Björkman, Zheng-Yong Liang, Ching-Hwa Ho, Ying-Sheng Huang, Po-Wen Chiu, Arkady V. Krasheninnikov, and Kazu Suenaga. Single-Layer ReS2: Two-Dimensional Semiconductor with Tunable In-Plane Anisotropy. *ACS Nano*, 9(11):11249–11257, November 2015. ISSN 1936-0851, 1936-086X. doi: 10.1021/acsnano.5b04851. URL http://pubs.acs.org/doi/10.1021/acsnano.5b04851.

[81] Hyejin Jang, Christopher R. Ryder, Joshua D. Wood, Mark C. Hersam, and David G. Cahill. 3d Anisotropic Thermal Conductivity of Exfoliated Rhenium Disulfide. *Advanced Materials*, 29(35):1700650, September 2017. ISSN 09359648. doi: 10.1002/adma.201700650. URL http://doi.wiley.com/10.1002/adma.201700650.

[82] Mathias Gehlmann, Irene Aguilera, Gustav Bihlmayer, Slavomír Nemšák, Philipp Nagler, Pika Gospodarič, Giovanni Zamborlini, Markus Eschbach, Vitaliy Feyer, Florian Kronast, Ewa Młyńczak, Tobias Korn, Lukasz Plucinski, Christian Schüller, Stefan Blügel, and Claus M. Schneider. Direct Observation of the Band Gap Transition in Atomically Thin ReS $_2$. *Nano Letters*, 17(9):5187–5192, September 2017. ISSN 1530-6984, 1530-6992. doi: 10.1021/acs.nanolett.7b00627. URL `http://pubs.acs.org/doi/10.1021/acs.nanolett.7b00627`.

[83] James L. Webb, Lewis S. Hart, Daniel Wolverson, Chaoyu Chen, Jose Avila, and Maria C. Asensio. Electronic bandstructure of ReS2 by high resolution angle resolved photoemission spectroscopy. *Physical Review B*, 96(11), September 2017. ISSN 2469-9950, 2469-9969. doi: 10.1103/PhysRevB.96.115205. URL `http://arxiv.org/abs/1704.06042`. arXiv: 1704.06042.

[84] Rui He, Jia-An Yan, Zongyou Yin, Zhipeng Ye, Gaihua Ye, Jason Cheng, Ju Li, and C. H. Lui. Coupling and Stacking Order of ReS $_2$ Atomic Layers Revealed by Ultralow-Frequency Raman Spectroscopy. *Nano Letters*, 16(2):1404–1409, February 2016. ISSN 1530-6984, 1530-6992. doi: 10.1021/acs.nanolett.5b04925. URL `http://pubs.acs.org/doi/10.1021/acs.nanolett.5b04925`.

[85] D. Biswas, Alex M. Ganose, R. Yano, J. M. Riley, L. Bawden, O. J. Clark, J. Feng, L. Collins-Mcintyre, M. T. Sajjad, W. Meevasana, T. K. Kim, M. Hoesch, J. E. Rault, T. Sasagawa, David O. Scanlon, and P. D. C. King. Narrow-band anisotropic electronic structure of ReS_2. *Physical Review B*, 96(8):085205, August 2017. ISSN 2469-9950, 2469-9969. doi: 10.1103/PhysRevB.96.085205. URL `https://link.aps.org/doi/10.1103/PhysRevB.96.085205`.

[86] Nur Baizura Mohamed, Keisuke Shinokita, Xiaofan Wang, Hong En Lim, Dezhi Tan, Yuhei Miyauchi, and Kazunari Matsuda. Photoluminescence quantum yields for atomically thin-layered ReS $_2$: Identification of indirect-bandgap semiconductors. *Applied Physics Letters*, 113(12): 121112, September 2018. ISSN 0003-6951, 1077-3118. doi: 10.1063/1.5037116. URL `http://aip.scitation.org/doi/10.1063/1.5037116`.

[87] Lewis Hart, Sara Dale, Sarah Hoye, James L. Webb, and Daniel Wolverson. Rhenium Dichalcogenides: Layered Semiconductors with Two Vertical Orientations. *Nano Letters*, 16(2):1381–1386, February 2016. ISSN 1530-6984, 1530-6992. doi: 10.1021/acs.nanolett.5b04838. URL http://pubs.acs.org/doi/10.1021/acs.nanolett.5b04838.

[88] Shishu Zhang, Nannan Mao, Na Zhang, Juanxia Wu, Lianming Tong, and Jin Zhang. Anomalous Polarized Raman Scattering and Large Circular Intensity Differential in Layered Triclinic ReS $_2$. *ACS Nano*, 11(10):10366–10372, October 2017. ISSN 1936-0851, 1936-086X. doi: 10.1021/acsnano.7b05321. URL http://pubs.acs.org/doi/10.1021/acsnano.7b05321.

[89] Sheng Yu, Hao Zhu, Kwesi Eshun, Chen Shi, Min Zeng, and Qiliang Li. Strain-engineering the anisotropic electrical conductance in ReS $_2$ monolayer. *Applied Physics Letters*, 108(19):191901, May 2016. ISSN 0003-6951, 1077-3118. doi: 10.1063/1.4947195. URL http://aip.scitation.org/doi/10.1063/1.4947195.

[90] Z.H. Zhou, B.C. Wei, C.Y. He, Y.M. Min, C.H. Chen, L.Z. Liu, and X.L. Wu. Anisotropic Raman scattering and mobility in monolayer 1t d -ReS 2 controlled by strain engineering. *Applied Surface Science*, 404:276–281, May 2017. ISSN 01694332. doi: 10.1016/j.apsusc.2017.01.305. URL https://linkinghub.elsevier.com/retrieve/pii/S0169433217303422.

[91] Yan-Ling Li, Yunguo Li, and Chunlin Tang. Strain engineering and photocatalytic application of single-layer ReS2. *International Journal of Hydrogen Energy*, 42(1):161–167, January 2017. ISSN 0360-3199. doi: 10.1016/j.ijhydene.2016.11.097. URL http://www.sciencedirect.com/science/article/pii/S0360319916333869.

[92] Yalan Yan, Chunlin Jin, Jia Wang, Tianru Qin, Fangfei Li, Kai Wang, Yonghao Han, and Chunxiao Gao. Associated Lattice and Electronic Structural Evolutions in Compressed Multilayer ReS $_2$. *The Journal of Physical Chemistry Letters*, 8(15):3648–3655, August 2017. ISSN 1948-7185. doi: 10.1021/acs.jpclett.7b01031. URL http://pubs.acs.org/doi/10.1021/acs.jpclett.7b01031.

[93] Naëmi Waeselmann. *Structural transformations in complex perovskite-type relaxor and relaxor-based ferroelectrics at high pressures and temperatures*. PhD thesis, University of Hamburg, 2012.

[94] Qianhui Zhang, Zhenyue Chang, Guanzhong Xu, Ziyu Wang, Yupeng Zhang, Zai-Quan Xu, Shujian Chen, Qiaoliang Bao, Jefferson Zhe Liu, Yui-Wing Mai, Wenhui Duan, Michael S. Fuhrer, and Changxi Zheng. Strain Relaxation of Monolayer WS_2 on Plastic Substrate. *Advanced Functional Materials*, 26(47):8707–8714, December 2016. ISSN 1616301X. doi: 10.1002/adfm.201603064. URL `http://doi.wiley.com/10.1002/adfm.201603064`.

[95] Nihar R. Pradhan, Amber McCreary, Daniel Rhodes, Zhengguang Lu, Simin Feng, Efstratios Manousakis, Dmitry Smirnov, Raju Namburu, Madan Dubey, Angela R. Hight Walker, Humberto Terrones, Mauricio Terrones, Vladimir Dobrosavljevic, and Luis Balicas. Metal to Insulator Quantum-Phase Transition in Few-Layered ReS $_2$. *Nano Letters*, 15(12): 8377–8384, December 2015. ISSN 1530-6984, 1530-6992. doi: 10.1021/acs.nanolett.5b04100. URL `http://pubs.acs.org/doi/10.1021/acs.nanolett.5b04100`.

[96] Dongbin Hou, Yanzhang Ma, Jianguo Du, Jinyuan Yan, Cheng Ji, and Hongyang Zhu. High pressure X-ray diffraction study of ReS2. *Journal of Physics and Chemistry of Solids*, 71(11):1571–1575, November 2010. ISSN 00223697. doi: 10.1016/j.jpcs.2010.08.002. URL `http://linkinghub.elsevier.com/retrieve/pii/S0022369710002416`.

[97] Yu-Cheng Kao, Tony Huang, Der-Yuh Lin, Ying-Sheng Huang, Kwong-Kau Tiong, Hsin-Yi Lee, Jhih-Min Lin, Hwo-Shuenn Sheu, and Chih-Ming Lin. Anomalous structural phase transition properties in ReSe $_2$ and Au-doped ReSe $_2$. *The Journal of Chemical Physics*, 137(2):024509, July 2012. ISSN 0021-9606, 1089-7690. doi: 10.1063/1.4733985. URL `http://aip.scitation.org/doi/10.1063/1.4733985`.

[98] Liliana Hromadová, Roman Martoňák, and Erio Tosatti. Structure change, layer sliding, and metallization in high-pressure MoS 2. *Physical Review B*, 87(14):144105, April 2013. ISSN 1098-0121, 1550-235X. doi:

10.1103/PhysRevB.87.144105. URL https://link.aps.org/doi/10.1103/PhysRevB.87.144105.

[99] Avinash P. Nayak, Swastibrata Bhattacharyya, Jie Zhu, Jin Liu, Xiang Wu, Tribhuwan Pandey, Changqing Jin, Abhishek K. Singh, Deji Akinwande, and Jung-Fu Lin. Pressure-induced semiconducting to metallic transition in multilayered molybdenum disulphide. *Nature Communications*, 5(1), December 2014. ISSN 2041-1723. doi: 10.1038/ncomms4731. URL http://www.nature.com/articles/ncomms4731.

[100] Zhao Zhao, Haijun Zhang, Hongtao Yuan, Shibing Wang, Yu Lin, Qiaoshi Zeng, Gang Xu, Zhenxian Liu, G. K. Solanki, K. D. Patel, Yi Cui, Harold Y. Hwang, and Wendy L. Mao. Pressure induced metallization with absence of structural transition in layered molybdenum diselenide. *Nature Communications*, 6(1):7312, November 2015. ISSN 2041-1723. doi: 10.1038/ncomms8312. URL http://www.nature.com/articles/ncomms8312.

[101] Tianshu Li and Giulia Galli. Electronic Properties of MoS $_2$ Nanoparticles. *The Journal of Physical Chemistry C*, 111(44):16192–16196, November 2007. ISSN 1932-7447, 1932-7455. doi: 10.1021/jp075424v. URL https://pubs.acs.org/doi/10.1021/jp075424v.

[102] H. Sahin, S. Tongay, S. Horzum, W. Fan, J. Zhou, J. Li, J. Wu, and F. M. Peeters. Anomalous Raman spectra and thickness-dependent electronic properties of WSe 2. *Physical Review B*, 87(16):165409, April 2013. ISSN 1098-0121, 1550-235X. doi: 10.1103/PhysRevB.87.165409. URL https://link.aps.org/doi/10.1103/PhysRevB.87.165409.

[103] Jingsi Qiao, Xianghua Kong, Zhi-Xin Hu, Feng Yang, and Wei Ji. High-mobility transport anisotropy and linear dichroism in few-layer black phosphorus. *Nature Communications*, 5(1):4475, December 2014. ISSN 2041-1723. doi: 10.1038/ncomms5475. URL http://www.nature.com/articles/ncomms5475.

[104] Demetrio Scelta, Adhara Baldassarre, Manuel Serrano-Ruiz, Kamil Dziubek, Andrew B. Cairns, Maurizio Peruzzini, Roberto Bini, and Matteo

Ceppatelli. Interlayer Bond Formation in Black Phosphorus at High Pressure. *Angewandte Chemie International Edition*, 56(45):14135–14140, November 2017. ISSN 14337851. doi: 10.1002/anie.201708368. URL http://doi.wiley.com/10.1002/anie.201708368.

[105] Taizo Sasaki, Kensuke Kondo, Yuichi Akahama, Satoshi Nakano, and Takashi Taniguchi. Raman spectroscopy of two-dimensional material under high pressure: Black phosphorus ultrathin film, phosphorene. *Japanese Journal of Applied Physics*, 56(5S3):05FB06, May 2017. ISSN 0021-4922, 1347-4065. doi: 10.7567/JJAP.56.05FB06. URL http://stacks.iop.org/1347-4065/56/i=5S3/a=05FB06?key=crossref.bc60912ffa3e9d2086e8d357a3b79ed2.

[106] F. Dybała, M. P. Polak, J. Kopaczek, P. Scharoch, K. Wu, S. Tongay, and R. Kudrawiec. Pressure coefficients for direct optical transitions in MoS2, MoSe2, WS2, and WSe2 crystals and semiconductor to metal transitions. *Scientific Reports*, 6(1), July 2016. ISSN 2045-2322. doi: 10.1038/srep26663. URL http://www.nature.com/articles/srep26663.

[107] Pengchao Lu, Joon-Seok Kim, Jing Yang, Hao Gao, Juefei Wu, Dexi Shao, Bin Li, Dawei Zhou, Jian Sun, Deji Akinwande, Dingyu Xing, and Jung-Fu Lin. Origin of superconductivity in the Weyl semimetal WT e 2 under pressure. *Physical Review B*, 94(22), December 2016. ISSN 2469-9950, 2469-9969. doi: 10.1103/PhysRevB.94.224512. URL https://link.aps.org/doi/10.1103/PhysRevB.94.224512.

[108] Avinash P. Nayak, Zhen Yuan, Boxiao Cao, Jin Liu, Junjie Wu, Samuel T. Moran, Tianshu Li, Deji Akinwande, Changqing Jin, and Jung-Fu Lin. Pressure-Modulated Conductivity, Carrier Density, and Mobility of Multilayered Tungsten Disulfide. *ACS Nano*, 9(9):9117–9123, September 2015. ISSN 1936-0851, 1936-086X. doi: 10.1021/acsnano.5b03295. URL http://pubs.acs.org/doi/10.1021/acsnano.5b03295.

[109] Nirup Bandaru, Ravhi S. Kumar, Daniel Sneed, Oliver Tschauner, Jason Baker, Daniel Antonio, Sheng-Nian Luo, Thomas Hartmann, Yusheng Zhao, and Rama Venkat. Effect of Pressure and Temperature on Structural Stability of MoS $_2$. *The Journal of Physical Chemistry C*, 118(6):

3230–3235, February 2014. ISSN 1932-7447, 1932-7455. doi: 10.1021/jp410167k. URL http://pubs.acs.org/doi/10.1021/jp410167k.

[110] M Karuzawa, M Ishizuka, and S Endo. The pressure effect on the superconducting transition temperature of black phosphorus. *Journal of Physics: Condensed Matter*, 14(44):10759–10762, November 2002. ISSN 0953-8984. doi: 10.1088/0953-8984/14/44/372. URL http://stacks.iop.org/0953-8984/14/i=44/a=372?key=crossref.23336d6464b3cba3612897e2cd85fd20.

[111] Y Akahama, M Kobayashi, and H Kawamura. Raman study of black phosphorus up to 13 GPa. *Solid State Communications*, 104(6):311–315, November 1997. ISSN 00381098. doi: 10.1016/S0038-1098(97)00325-6. URL http://linkinghub.elsevier.com/retrieve/pii/S0038109897003256.

[112] Satyendra Nath Gupta, Anjali Singh, Koushik Pal, Biswanath Chakraborti, D. V. S. Muthu, U. V. Waghmare, and A. K. Sood. Raman anomalies as signatures of pressure induced electronic topological and structural transitions in black phosphorus: Experiments and Theory. *Physical Review B*, 96(9), September 2017. ISSN 2469-9950, 2469-9969. doi: 10.1103/PhysRevB.96.094104. URL http://arxiv.org/abs/1612.06135.

[113] Z.J. Xiang, G.J. Ye, C. Shang, B. Lei, N.Z. Wang, K.S. Yang, D.Y. Liu, F.B. Meng, X.G. Luo, L.J. Zou, Z. Sun, Y. Zhang, and X.H. Chen. Pressure-Induced Electronic Transition in Black Phosphorus. *Physical Review Letters*, 115(18), October 2015. ISSN 0031-9007, 1079-7114. doi: 10.1103/PhysRevLett.115.186403. URL https://link.aps.org/doi/10.1103/PhysRevLett.115.186403.